2016

Numerical modeling of ambient noise seismic interferometry

Simisola M. Arogundade
Michigan Technological University, sarogund@mtu.edu

NUMERICAL MODELING OF AMBIENT NOISE SEISMIC INTERFEROMETRY

By

Simisola M. Arogundade

A THESIS

Submitted in partial fulfillment of the requirements for the degree of

MASTER OF SCIENCE

In Geophysics

MICHIGAN TECHNOLOGICAL UNIVERSITY

2016

This thesis has been approved in partial fulfillment of the requirements for the Degree of MASTER OF SCIENCE in Geophysics.

Department of Geological and Mining Engineering and Sciences

Thesis Co-Advisor: *Dr. Wayne D. Pennington*

Thesis Co-Advisor: *Dr. Roohollah Askari*

Committee Member: *Dr. Roger M. Turpening*

Department Chair: *Dr. John S. Gierke*

Table of contents

List of Figures

Preface

Seismic exploration involves data acquisition, processing and interpretation. This thesis submitted for the degree of Masters of Science at the Michigan Technological University focused on the understanding a cost effective method of data acquisition compared to the conventional method and also data processing.

I generated and analyzed the results presented in this thesis under the supervision of Dr. Wayne D. Pennington and Dr. Roohollah Askari in the Department of Geological and Mining Engineering and Sciences. Technical expertise was also provided by Dr. Wayne D. Pennington and Dr. Roohollah Askari during the research and also when writing the paper.

This work contains material that is in preparation for submission to a conference proceeding.

Acknowledgement

My deepest gratitude to Dr. Wayne D. Pennington and Dr. Roohollah Askari, my research advisors, for their patient guidance, enthusiastic encouragement and useful critiques of this research work. You always been my inspiration towards excellence and for this, I am very grateful.

I would also like to offer my special thanks to my committee member Dr. Roger M. Turpening for their helpful guidance and suggestions.

I want to thank the Dr. Jan Thorbecke at Delft University of Technology, Netherlands, who created the Finite difference modeling codes, which aims at the modeling of measurements used for Seismic Interferometry. In addition, I am grateful to Him and Boris Boullenger for their assistance and willingness to give their time so generously.

To Federica Lanza, thanks for being a good mentor and for your support during my graduate research.

I wish to thank Dr. Gowtham for his valuable technical support on this project.

I also want to express my appreciation to the members of African Students Organization for their help and encouragements.

Most importantly, I want to express my heartfelt appreciation to my parents,

Bamidele and Benjamin Arogundade, and my boyfriend, Olumide Winjobi. There have been numerous occasions where I remember feeling disheartened and stumped about the direction of my research, but your love, support and understanding reinvigorates my enthusiasm and raise my spirits immeasurably. I love you and bless you forever.

Beyond this, I want to thank God for being such a loving and merciful Father.

1. Abstract

CO_2 sequestration involves storing CO_2 in a deep geological formation and may help to mitigate the increasing emission of carbon. To monitor the migration of injected fluid in the reservoir, seismic observations may be used to observe changes in reflection character. Conventional methods to image the subsurface, using active seismic measurements, with man-made sources, have been applied at a few test sites, and the use of passive measurements, with natural sources, has been considered as a probable cost-efficient method to monitor CO_2 migration and leakage. This numerical modeling study examines the use of seismic interferometry to retrieve weak seismic reflections from background noise, a form of passive monitoring.

The factors that influence the quality of the retrieved reflections from interferometry include geophone interval, geophone depth, and effect of shallow noise sources, assuming we seek reflections from deep noise sources, representing either teleseismic events or local events as expected in a field of active injection. Using model data, geophone interval had no significant effect on the reflection quality, but buried geophones produce ghost reflections, suggesting that shallow geophones might be optimal. Shallow noise sources produce a destructive effect on the reflections from deeper noise sources and damage the resulting image.

2. [1]Introduction

Fossil fuels meet 80% of the world's energy demand (IEA 2015). Since the mid-19th century industrial revolution, 290 gigatons of carbon (GtC) have been released into the atmosphere, 90% of which comes from fossil fuel combustion (IEA 2015, Lackner 2003). Also, the increasing of carbon emissions at a rate of 1.2% per year over the past decade and, in particular, an accelerated increment to 2.3% between 2000 and 2014. Several methods have been implemented to reduce the emission of carbon: use of renewable energy, nuclear power, low carbon fossil fuel (e.g. natural gas instead of coal), decarbonisation of fuel and flue gases and carbon sequestration.

CO_2 geologic sequestration is the process of storing CO_2 in a geological formation. Although underground CO_2 injection is a proven technique, which also applies to enhanced oil recovery, some challenges should be addressed to make it more appealing for sequestration, such as long-term leakage, seismic instability, and potential migration of buoyant CO_2. Lackner (2003) describes CO_2 sequestration as the best alternative until other inexpensive, clean and plentiful technologies are available. Using active seismic measurements, with man-made sources, numerous studies have been conducted to investigate some of these challenges above and the effect of CO_2 injection on the elastic properties of the geological formation. These studies include using non-seismic methods (Sherlock et al. 2006); seismic methods and rock physics modeling (Arts et al. 2004), time-lapse seismic survey (Ivandic et al. 2013), and cross-well seismic methods (Harris et al.

[1] The materials contained in this thesis is in preparation for submission to a conference proceeding.

1995) . Although non-seismic methods such as gravity and electrical methods are lower-cost supplement method of monitoring CO_2 sequestration compare to seismic methods, they are faced with challenges that undermine their results compared to seismic methods. For instance, injecting CO_2 lowers the bulk density of the reservoir, thereby decreasing the gravitational response. Meanwhile, seismic method measures both density and elastic moduli, and this enables us to investigate changes in seismic reflected amplitudes, which can then be used to study changes in pressure and saturation based on rock physics models. To this aim, time-lapse seismic survey, on the other hand, is used to monitor pressure and saturation changes over time during CO_2 production or injection. Although a time-lapse survey over a CO_2 storage field is efficient in providing us with information about changes in the targeted reservoir, it can be costly. Also, since seismic stations are not usually permanently installed, the fold acquired and azimuthal coverage for each repeated measurement can be affected due to reasons such as constraints from roads and infrastructures (Ivandic et al. 2013). However to minimize some of these issues, Boullenger et al. (2015) studied time-lapse seismic surveys using passive seismic sources instead of active seismic surveys Passive seismic surveys require no active source but makes use of natural “noise” sources. Unlike active measurements, the seismic stations are permanently installed, and, therefore, the same spread of receivers is used and this is very advantageous to the repeatability of the survey. As a result, passive seismic measurements are expected to be cost effective compared to active seismic measurements. In order to image the subsurface structure from passive seismic measurements, noise recordings from different receiver locations are cross-correlated to retrieve reflection images, a process called seismic interferometry (SI).

Seismic interferometry is a process where reflection images are generated by cross-correlation of ambient noise. The technique of interferometry was first applied in radio astronomy to radio signals from cosmic sources (Thompson, Moran, and Swenson Jr 2008) and since then, the use of seismic interferometry to retrieve Green's function has been used in various fields such as seismology, and engineering. Claerbout (1968) used a 1D reciprocity theorem to auto-correlate transmission responses from subsurface sources in order to retrieve reflected responses of the same medium. Claerbout also proposed a 3D scenario, by cross correlating two noise traces recorded at two geophone locations such that the retrieved reflection response is recorded at one geophone location while the other location acts as a virtual source.

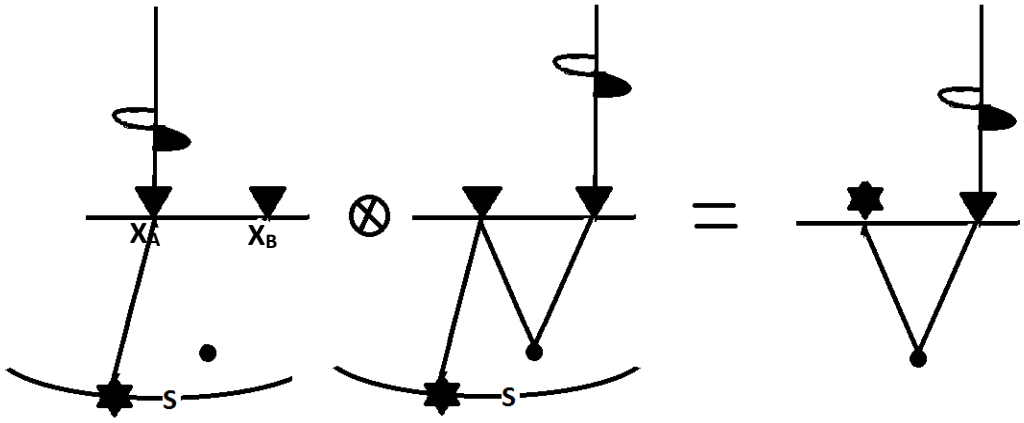

Figure 1: Schematic description of seismic interferometry (SI) where S is the source boundary and $\otimes$ is the cross-correlation sign. The location of the receivers are x_A and x_B assuming the medium is lossless. $\widehat{G}(x_B, x, \omega)$ and $\widehat{G}(x_B, x, \omega)$ are the receivers' response at the location x_A and x_B respectively. The impulse response observed after cross correlation is the response observed if a source was placed at x_A. Adapted from Wapenaar et al. (2010)

Figure 1 presents the schematic description of seismic interferometry. It shows sources at boundary S generating seismic waves wahich are recorded by the receivers at location x_A and x_B, assuming the medium is lossless and the propagation velocity is constant. Since

the ray path to each receiver from the source is common to both receivers, the signal associated with that path cancels out during the cross correlation process, leaving the path $x_B - x_A$ between the two receivers. When the responses observed at the receiver locations are cross correlated, cross correlation seismogram (retrieved Green's function) can be interpreted as the impulse observed at the source location at x_B as if the source is placed at x_A.

Seismic interferometry applies to both passive and controlled seismic measurements. This paper will focus on ambient-noise seismic interferometry (ANSI), which is described as a passive seismic measurement. This methodology can be used for a time-lapse survey to study and monitor CO2 sequestration. However, to gain a proper understanding of ANSI, we present a numerical forward modeling approach to a passive seismic measurement to retrieve reflected response and study the factors that could affect the quality of the retrieved reflected response such as:

- Geophone depth
- Geophone interval
- Shallow noise sources (representing coherent noise)

3. Theory

3.1. Green's Function for Seismic Interferometry Two-way Wavefield

Assuming a lossless 1D homogenous media, Claerbout (1968) proved that a reflection response can be reconstructed from the transmission response from subsurface sources using the one-way reciprocity theorem. Further, Wapenaar and Fokkema (2006) derived the relation below using two-way wavefield reciprocity theorem of the correlation type assuming a lossless homogeneous fluid medium, smoothly varying medium, and an impulsive source.

$$\hat{G}(x_B, x_A, \omega) + \hat{G}^*(x_B, x_A, \omega) \approx \frac{2}{\rho c} \oint_S \hat{G}^*(x_A, x, \omega)\, \hat{G}(x_B, x, \omega) d^2x \qquad (1)$$

where S is a closed surface, x is the source coordinate; x_A and x_B are the geophone locations at the surface; ρ is the mass density and c is the propagation velocity. $\hat{G}(x_B, x_A, \omega)$ denotes the Green's function observed at x_B from a source at x_A while $\hat{G}^*(x_B, x_A, \omega)$ is the time reversal of the Green's functions observed at x_B from a source at x_A. Equation 1 assumes that the boundary, S, is a sphere with a large radius and that all rays are normal to the boundary, which allows dipole sources to be replaced with monopole sources. These assumptions involve amplitude errors that can be significant and produce spurious arrivals (Wapenaar and Fokkema 2006). However, since the phase of the signal is not affected, equation 1 can still be used for SI. If the sources are mutually uncorrelated, noise sources

and their power spectra are the same for all noise sources at all x coordinates, the noise signatures become

$$\langle \widehat{N}^*(x',\omega)\widehat{N}(x,\omega)\rangle = \delta(x-x')\hat{S}(\omega) \qquad (2)$$

where $\widehat{N}(x,\omega)$ represents the noise spectrum at x, $\hat{S}(\omega)$ is the power spectrum of a noise source, and $\langle\,.\,\rangle$ is the spatial ensemble average. Therefore, for mutually uncorrelated noise sources, equation 1 is modified to give

$$\left\{\hat{G}(x_B,x_A,\omega) + \hat{G}^*(x_A,x_B,\omega)\right\}\hat{S}(\omega) \approx \frac{2}{\rho c}\langle \hat{p}^{obs*}(x_A,\omega)\,\hat{p}^{obs}(x_B,\omega)\rangle \qquad (3)$$

Since $2/\rho c$ has no effect on the phase of the retrieved Green's functions in ANSI, equation 3 will be rewritten to give

$$\left\{\hat{G}(x_B,x_A,\omega) + \hat{G}^*(x_A,x_B,\omega)\right\}\hat{S}(\omega) \approx \langle \hat{p}^{obs*}(x_A,\omega)\,\hat{p}^{obs}(x_B,\omega)\rangle \qquad (4)$$

$$\langle \hat{p}^{obs*}(x_A,\omega)\,\hat{p}^{obs}(x_B,\omega)\rangle = \oint_S \hat{G}^*(x_A,x,\omega)\,\hat{G}(x_B,x,\omega)\hat{S}(\omega)d^2x$$

Where $\hat{p}^{obs*}(x_A,\omega)$ and $\hat{p}^{obs}(x_B,\omega)$ are the observed wavefields recorded at x_A and x_B

Equation 4 is the cross-correlation of seismic responses from receivers x_A and x_B with the autocorrelation of the noise source function $\hat{S}(\omega)$ with the assumption that the sources are uncorrelated, randomly distributed and that the medium is lossless. This yields the retrieved response between two receivers and is assumed to be similar to the response from a source placed at the location of one of the receivers.

4. Methodology

Synthetic passive seismic traces were generated using a 2D finite difference (FD) acoustic modeling scheme introduced by Thorbecke and Draganov (2011), assuming no attenuation or dispersion. This program is an open source code that uses Seismic UN*X to output files. (The code can be downloaded directly from http://janth.home.xs4all.nl/Software/Software.html). The receiver positions were assumed to also be the locations of virtual seismic sources (shots). After the FD modeling, each trace was cross-correlated with all other traces and then processed to image the subsurface. The cross-correlation of the (long) recordings between one receiver and each of the others results in a common virtual-source gather, and the reflection events obtained are referred to as retrieved reflections. Examples that provide details will be presented in the following section.

5. Numerical Results

The 2D finite difference (FD) acoustic modeling scheme introduced by Thorbecke and Draganov (2011) was used to generate an acoustic data model for randomly distributed sources (figure 2). The model is 2500m wide and 2500m deep; numbering is from left to right in the images shown, and from shallow to deep. There are 100 “noise” sources with an average duration of 2 s, a maximum frequency of 20 Hz occurring over a total modeling time of 400 s; they are distributed randomly within that time, and randomly within a region near the base of the model. For the initial model, 200 vertical-component geophones lie

10m below the surface, with 4m spacing, centered at the middle of the model (from 850m to 1650m).

Figure 3 shows all of the 100 source signatures, each with varying source duration (up to 2s), and examples of one source and its amplitude spectrum. The noise source signature shown in Figure 3b was created by randomly setting values for amplitude and phase up to the defined maximum frequency of 20Hz (Thorbecke and Draganov 2011). The beginning and the end of the noise signal is smoothly extrapolated to avoid dispersion and to suppress frequencies above the defined maximum frequency (Appendix A). In the example presented in Figure 2, the only source of acoustic energy is the deep "sources"; in later examples, coherent noise is simulated by shallow discrete sources (intended to resemble traffic, industrial, or wind noise). Note that the acoustic energy recorded as a seismogram at each receiver is the superposition of the mutually uncorrelated noise sources presented here.

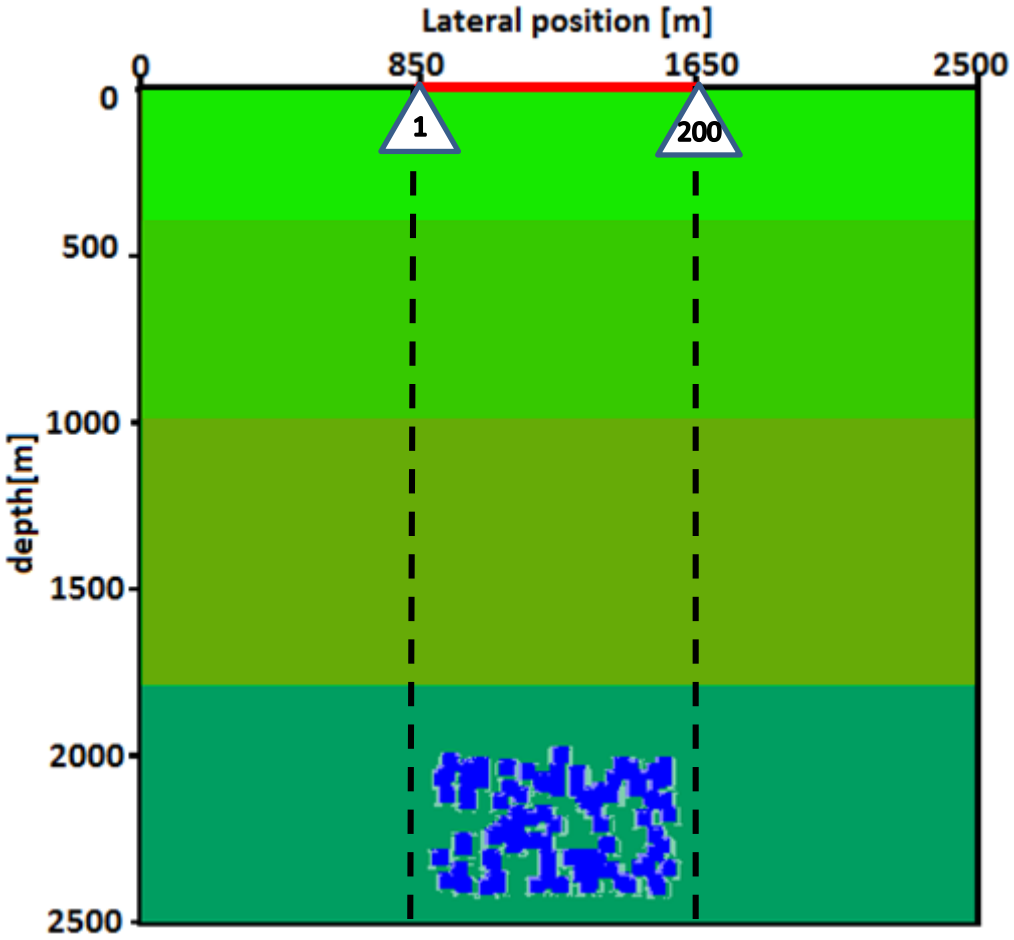

Figure 2: an Acoustic model of randomly distributed noise sources. The two triangles represent the 1st and the 200th receivers. The blue squares represent 100 deep noise sources. The red line represents the 800 m receiver line with receiver interval of 4m, at 10m depth. The black dashed lines define the lateral area within which the deep passive sources are generated. The different shades of green indicate different layers with a constant velocity as indicated in Table 1.

Table 1: Geologic model for figure 2

Thickness (m)	Depth of top (m)	Velocity (m/s)	Density (kg/m^3)
400	0	1500	1000
600	400	2000	1400
800	1000	2900	1500
700	1800	3900	1800

a)

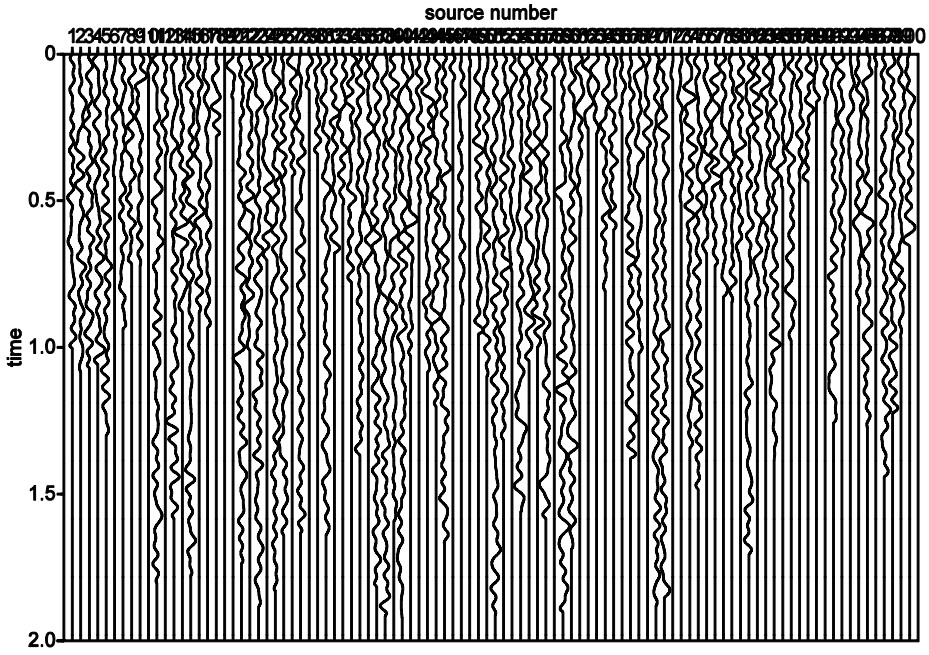
source number
time
0
0.5
1.0
1.5
2.0

b)

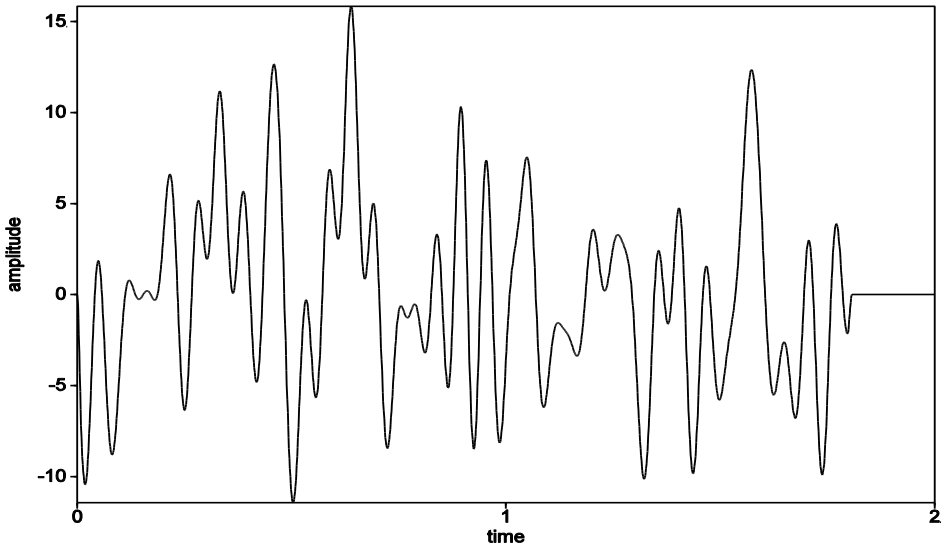
amplitude
time
15
10
5
0
-5
-10
0
1
2

c)

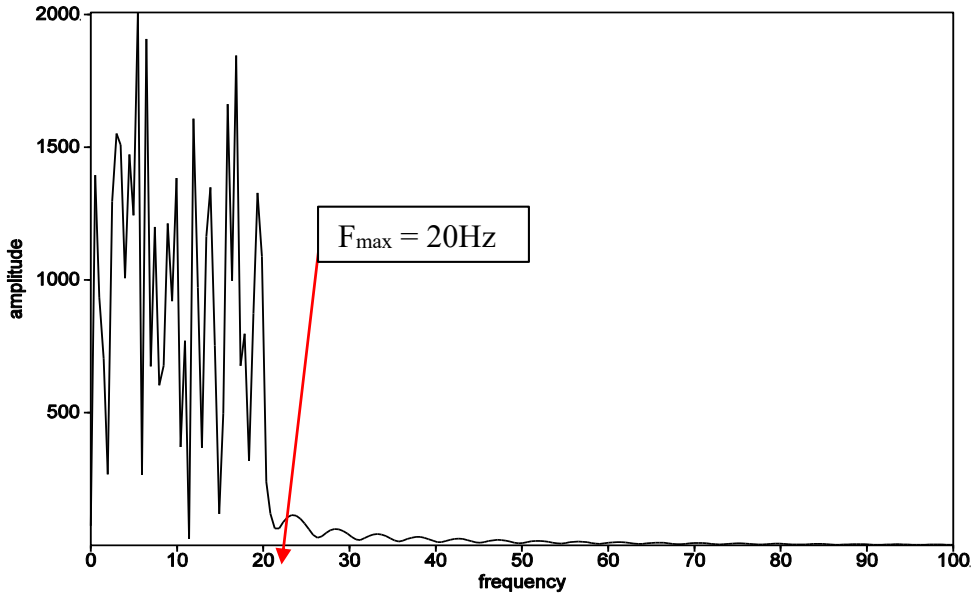

Figure 3: (a) The 100 random noise signatures with varying source duration and the noise frequency spectrum of the signal. (b) One source signature in detail. (c) The amplitude spectrum of the source signature in 3(b).

For computing efficiency, there is a limit of 16384 time samples that can be written in a file, or "panel." To accommodate the full 400s of noise signal generated in the model, six noise panels of 65s and one of 10s were created with a sample rate of 0.004 samples/s. For all of the analyses in this study, the six 65s panels were used. Figure 4 shows one of the panels with selected time windows and receivers.

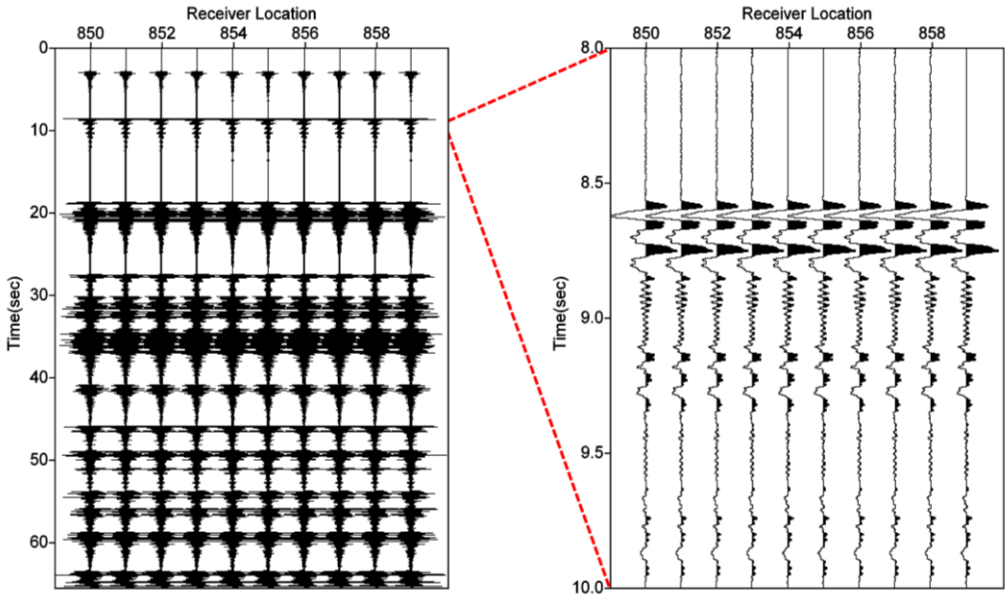

Figure 4: On the left side, a 9-trace 65s "noise panel." For display purposes, the left-most nine receivers (of 200) are shown labeled by their location. On the right side is an expanded view of a short time window.

To retrieve reflections from these noise panels, every receiver position in a noise panel can be assumed to represent a virtual shot position. Each trace represents a master trace which will be cross-correlated with all other traces to obtain a "correlation panel" for that master trace; this is, in effect, a common virtual-shot gather with the virtual shot location at the location of the master trace. With 200 receiver locations, we obtain 200 common virtual-shot gathers. In order to improve the strength of the signal, and to better simulate real-world conditions of continuous recording over time, this procedure was repeated for all six noise panels. Then the six correlation panels were stacked. The result is 200 common virtual-shot gathers, one for each of the receiver locations. Because there is a nearly perfect correlation for nearby traces at zero lag, regardless of reflector location, we consider these to be "correlation artefacts" and early times were muted before sorting into common mid-point (CMP) gathers. The reflections from deeper horizons exhibit weaker amplitudes due

to geometric spreading; in order to visually observe these at similar amplitudes, we applied a time-dependent gain to the common shot gathers, CMP gathers, and the stacked sections as they are presented in this paper. The time-dependent gain we used for all figures was obtained by multiplying the amplitude of each sample within a trace by a power of time (t^{tpow}, where tpow=0.2). Figure 5a and 5b show a common virtual shot gather for a virtual shot location of 850 m (receiver number 1 shown in figure 2) before muting and after muting. Figure 5c also shows the zoomed in common shot gather after muting to display the move-out of each reflector. We observed from figure 5c that the move-out of the reflectors are less steep, which is as a result of the depth of our sources.

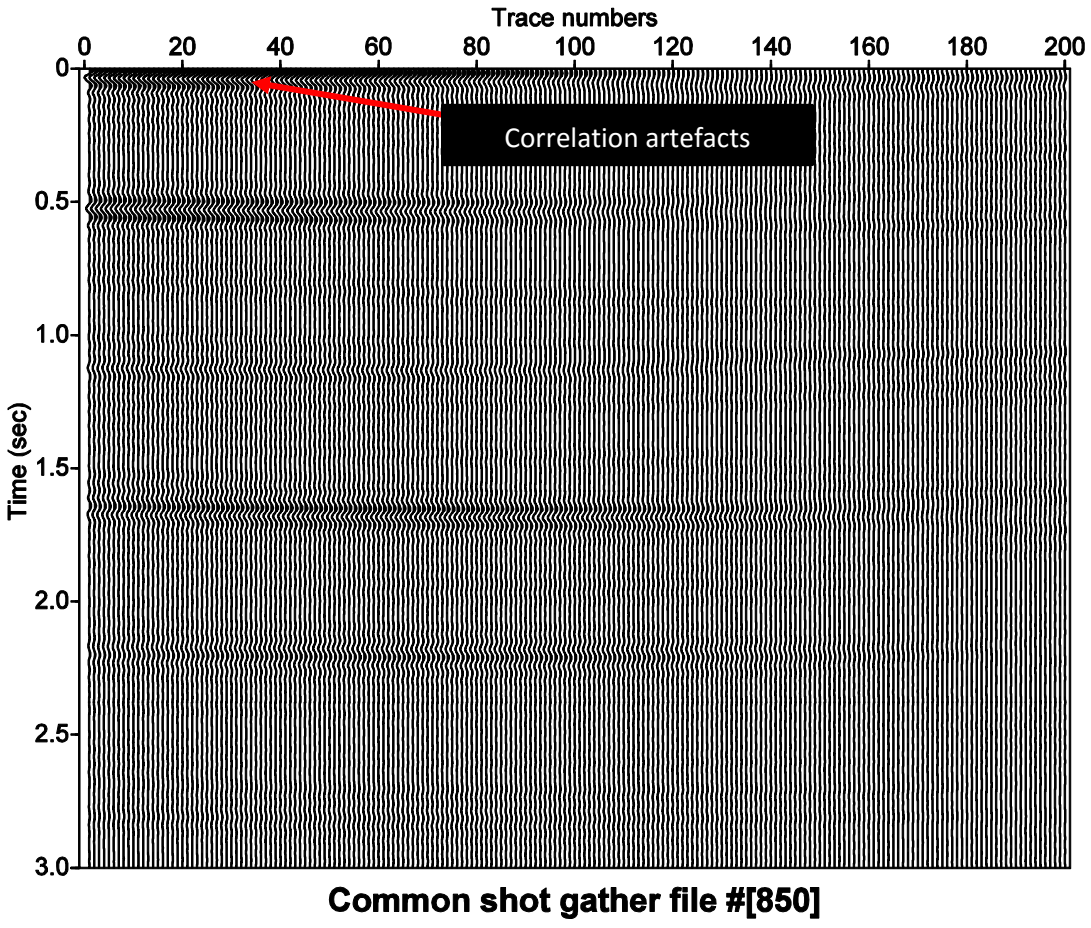

b)

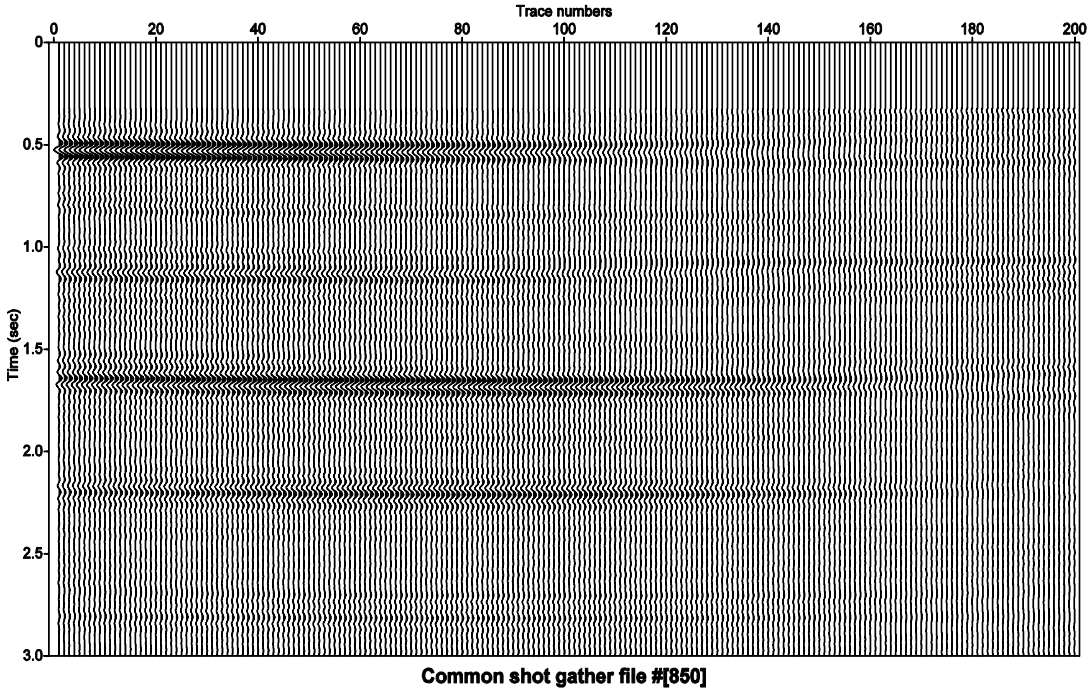
Trace numbers
0
20
40
60
80
100
120
140
160
180
200
Time (sec)
0
0.5
1.0
1.5
2.0
2.5
3.0
Common shot gather file #[850]

c)

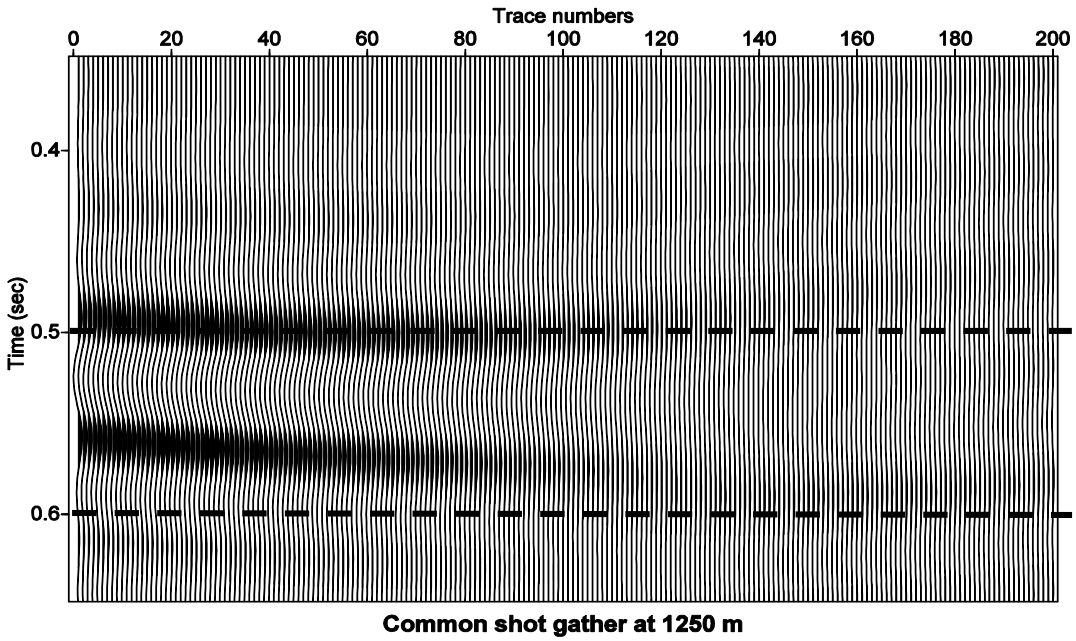

Figure 5: Common shot gather at 850 m virtual shot position (receiver number 1 presented on Figure 2). The result in a) shows the presence of "correlation artifacts" resulting from the nearly perfect correlation at zero lag The result in b) shows the same gather after muting the correlation artifacts. The result in c) shows details for the 0.5s reflection arrivals to demonstrate its moveout. [To boost the signals for display, a time-dependent gain was applied to this and to the other gathers and stacked sections presented later as explained in the text]. In this paper, shot gathers and CMP gathers are displayed as wiggle traces, as here, while sections (of stacked traces) will be displayed in variable density, as in Figure 7.

The 200 common shot gathers were sorted into common midpoint (CMP) gathers. To suppress multiples, CMP gathers are usually stacked after correcting for normal moveout (NMO), the amount of travel time required for reflections at non-zero offset through an oblique path compared to the normal-incidence trace (Buchholtz 1972). To determine the normal move-out correction, a stacking velocity for each gather was determined using usual techniques. The stacking velocity for a horizontally layered model should be approximately equal to the computed "RMS" velocity (see Appendix for details of these

procedures). Table 2 displays the stacking velocity and the computed RMS velocity with a summary of the geologic model presented in Figure 2.

Table 2: The comparison of the stacking velocity and the predicted RMS velocity. Also, it shows the summary of the geologic model presented in Figure 2.

Thickness of layer (m)	Depth to top of layer (m)	Time within the layer (s)	Interval Velocity (m/s)	Density (kg/m^3)	Stacking velocity at the base reflector (m/s)	Computed RMS velocity at the base reflector (m/s)
400	0	0.53	1500	1000	1509.4	1500.0
600	400	0.60	2000	1400	2250.1	1782.3
800	1000	0.55	2900	1500	2920.5	2211.3
700	1800	0.36	3900	1800	3929.5	2588.9

In this study, the stacking velocities did not agree with the predicted RMS velocity, so we will expect the presence of multiples in our stacked section and also a poor stacking section. An explanation for the differences between our stacking and RMS velocities might be as a result of the short acquisition aperture. This means that a more accurate NMO correction can be applied if the acquisition aperture is increased (See Appendix A). Figure 6 shows an example CMP gather, and Figure 7 displays the stacked section after velocity analysis, NMO correction, and stacking.

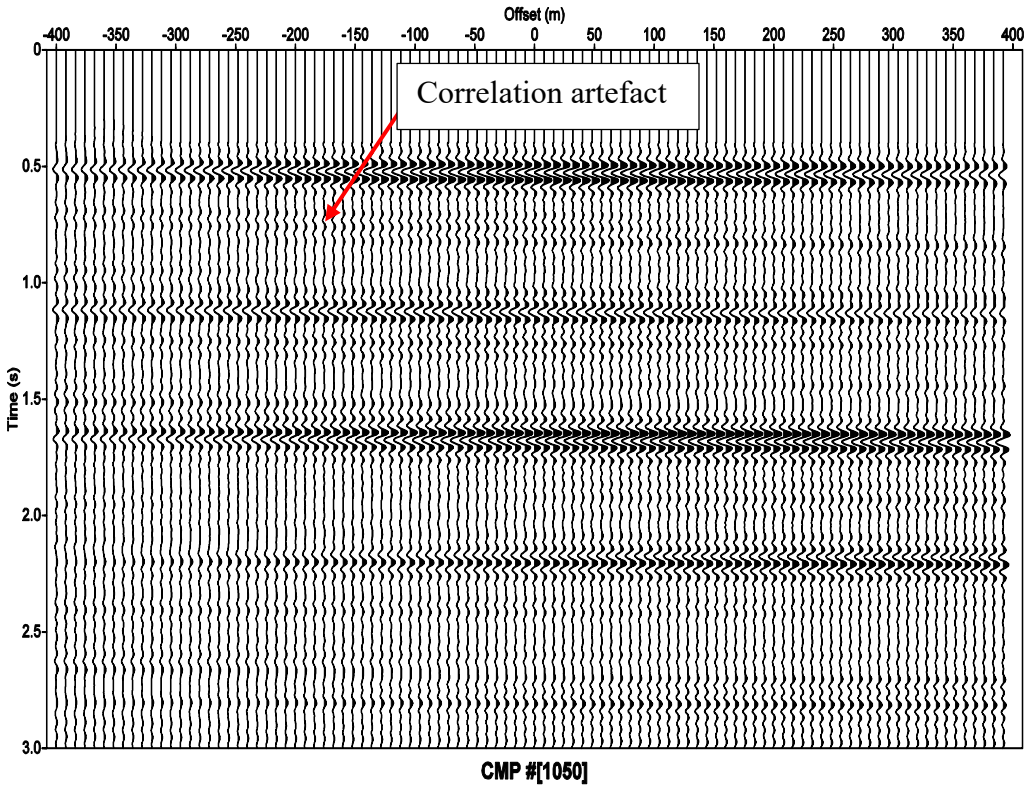

Figure 6: An example of a common midpoint gather, prior to NMO correction.

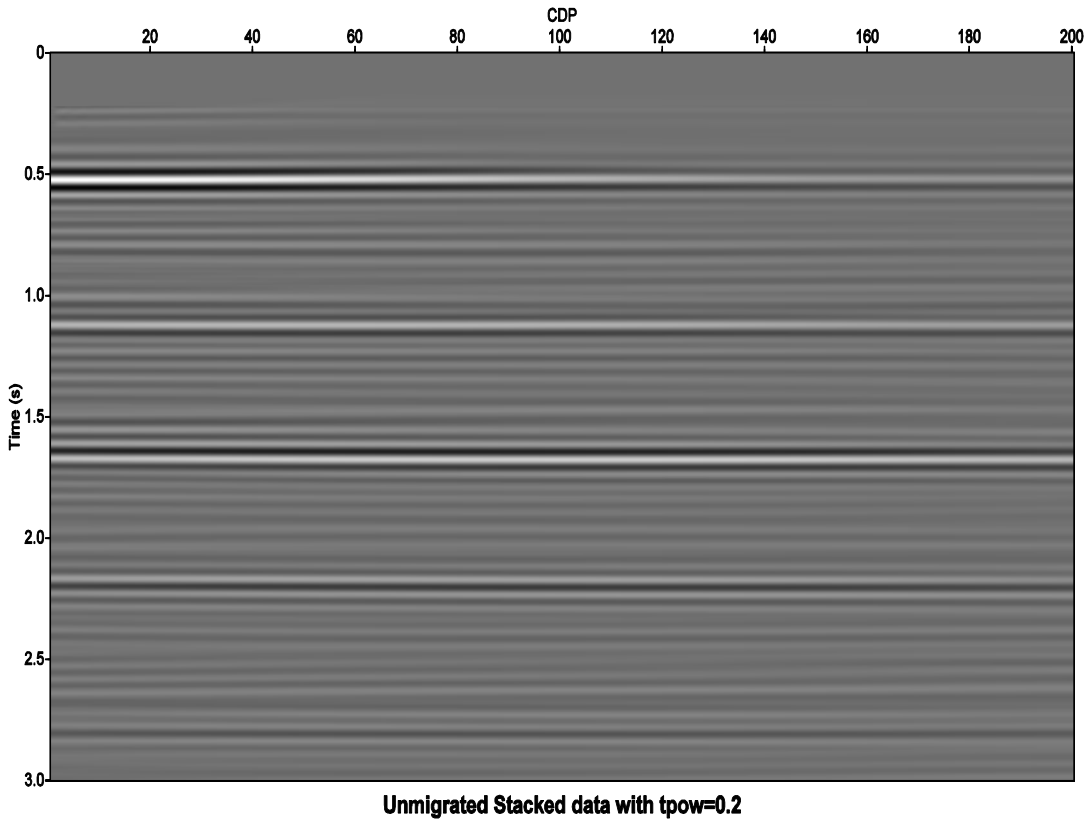

Figure 7: Unmigrated stacked section after velocity analysis.

Although figure 6 shows the presence of correlation artefacts, they show the potential of ANSI to retrieve reflections. However, to reduce these artefacts and produce better results, we will need to increase the number of sources to increase the signal-to-noise ratio, and applying deconvolution.

5.1. Influence of Geophone Interval

In this section, we analyze results from 4m, 8m and 16m geophone intervals for signal quality. Before cross correlation, 20% random noise was added to the noise panels that had been generated using the 4m geophone interval model (figure 2). To ensure identical

random noise was applied to models using 4m, 8m, and 16m geophone intervals, we simply decimated the noise panels that had been created with random noise, removing alternating records from 4m geophone interval simulation, and then did it again, resulting in records with 8m and 16m geophone intervals. The rest of the processing was identical. The velocity analysis was repeated independently in each case, to provide greater similarity to real-world conditions. To show the comparison between the CMP gathers obtained between 4m, 8m, and 16m geophone interval, we display the CMP gathers at the same location (Figure 8).

a)

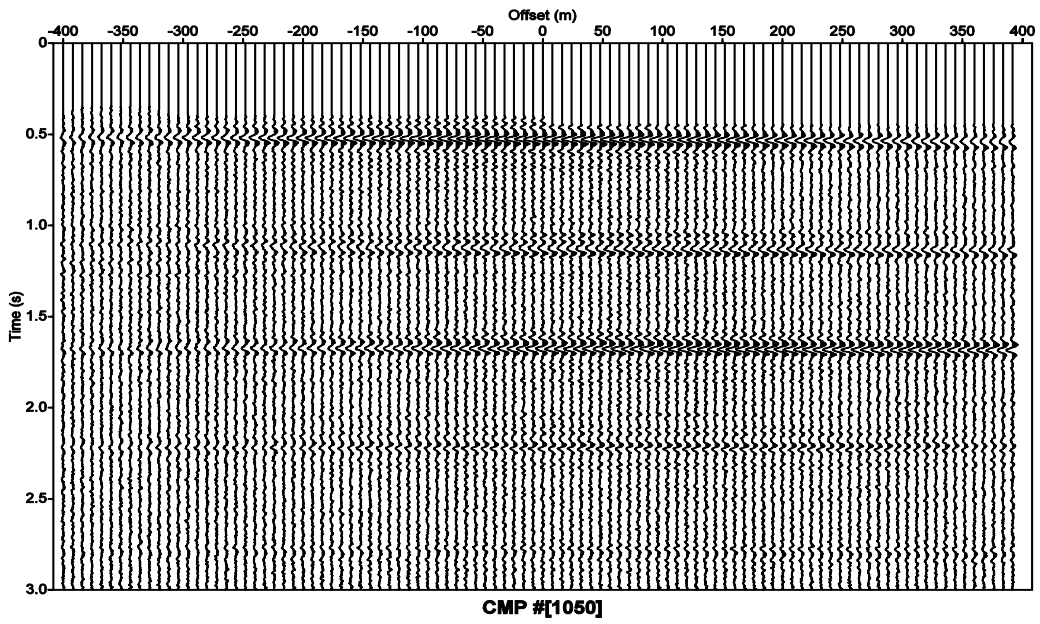

b)

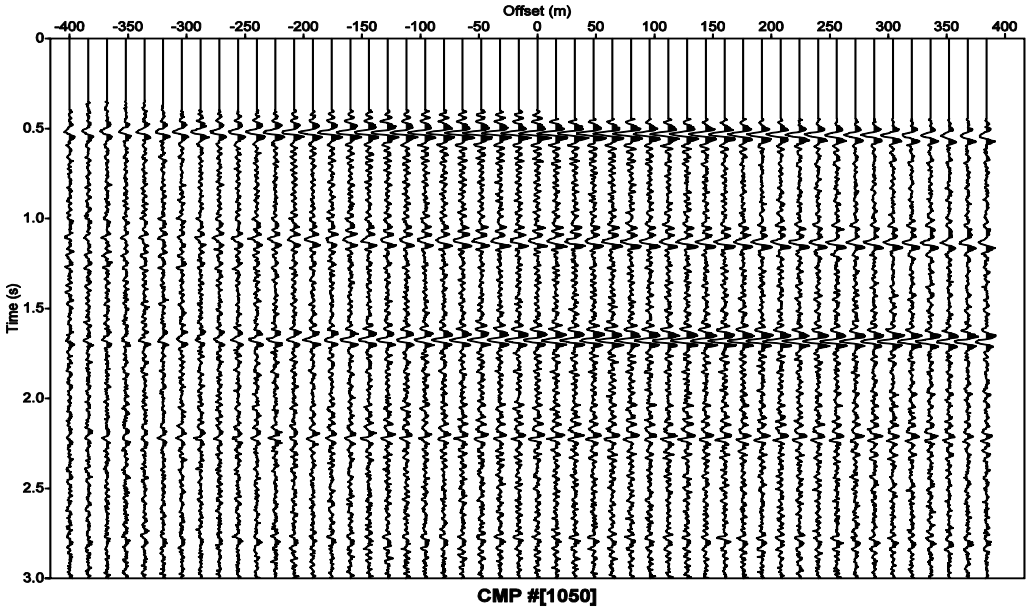

c)

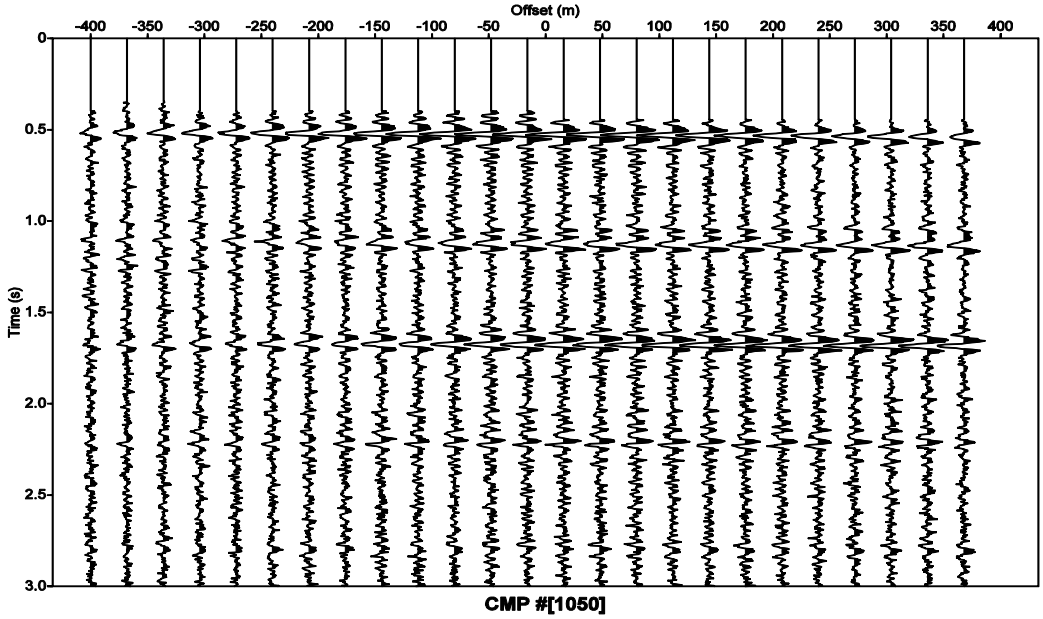

Figure 8: Comparison of the common midpoint gather with 20% signal to noise ratio added for a) 4m geophone interval b) 8m geophone interval c) 16m geophone interval.

These results show that geophone spacing may not have a significant effect on the quality of the final image when the geology structures are simple. Our results also express some encouragement that few recording stations would be required in areas of simple geological structures, thereby reducing the cost of field deployment.

5.2. Influence of Geophone Depth

Using the same model parameters presented in Figure 2, we repositioned the geophones from 10 m to 50 m depth to observe the effect of buried geophones on the quality of the retrieved reflections. Figure 9 shows a common virtual shot gather with geophones at 50 m depth (at 850 m virtual shot location; receiver number 1 illustrated in figure 2). Figure 10 shows the comparison between a CMP gather with geophones at 10 m depth and at 50 m depth. The differences are clearly associated with ghosting (the interference between the directly recorded reflection arrival and that which immediately follows, after reflection from the free surface).

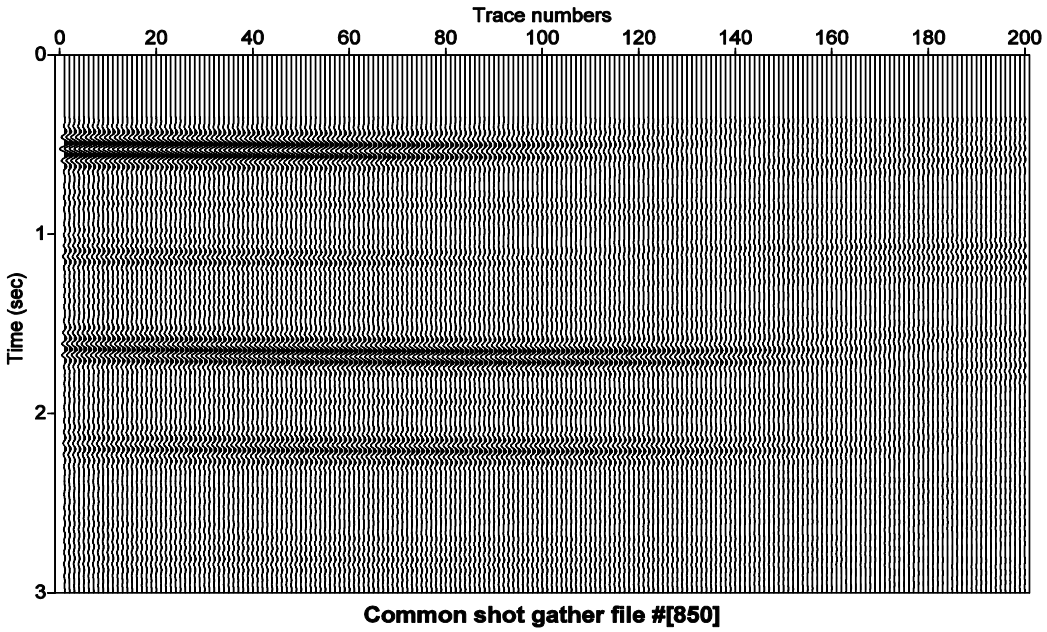

Figure 9: Common virtual shot gather at 850 m shot position

a)

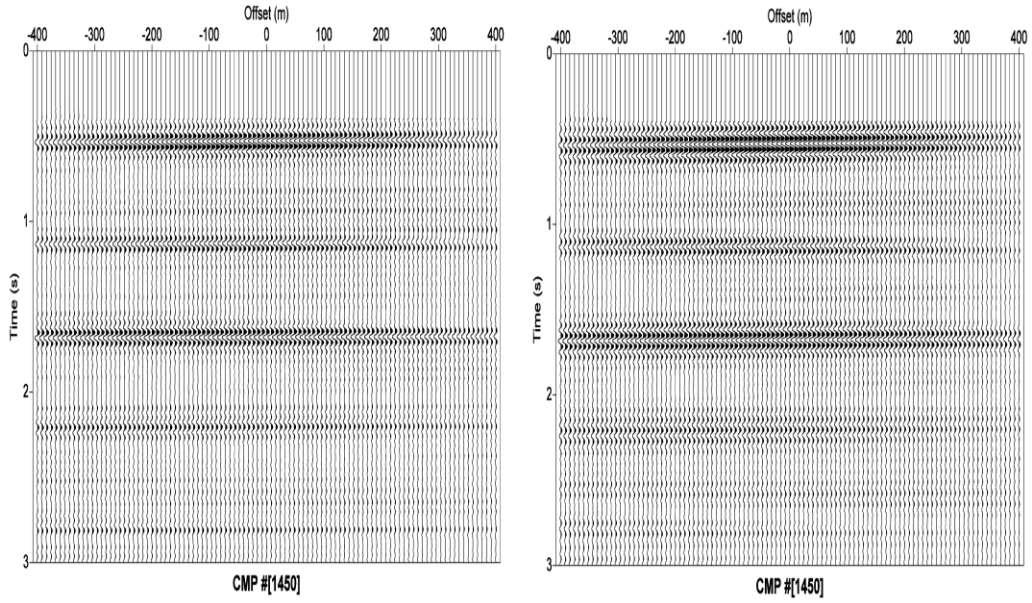
Offset (m)
-400 -300 -200 -100 0 100 200 300 400
Time (s)
0 1 2 3
CMP #[1450]
Offset (m)
-400 -300 -200 -100 0 100 200 300 400
Time (s)
0 1 2 3
CMP #[1450]

b)

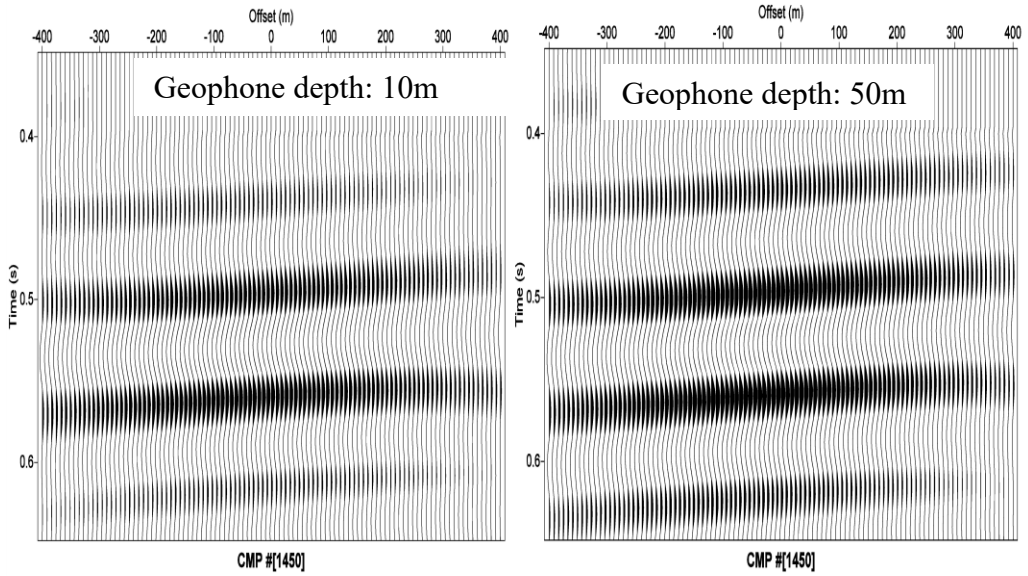
Offset (m)
-400 -300 -200 -100 0 100 200 300 400
Geophone depth: 10m
Time (s)
0.4 0.5 0.6
CMP #[1450]
Offset (m)
-400 -300 -200 -100 0 100 200 300 400
Geophone depth: 50m
Time (s)
0.4 0.5 0.6
CMP #[1450]

c)

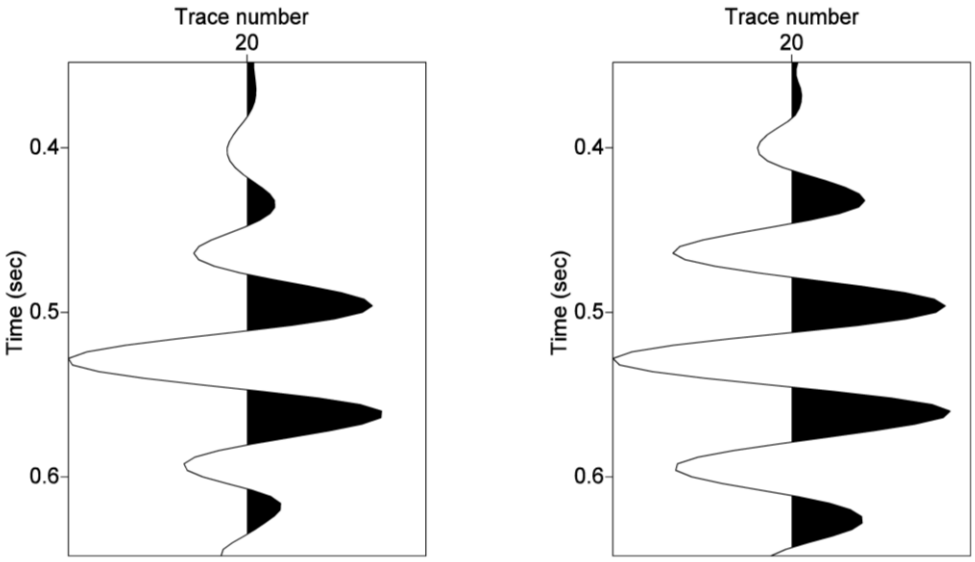

Figure 10: The comparison between a CMP gather with geophones at 10 m depth and at 50 m depth CMP gather. The results in a) shows the comparison between a CMP gather obtained with geophones at 10m depth (left side) and 50 m depth (right side), b) show a single reflector at 0.5s from both examples in the figure above, c) shows the shows the comparison between two traces obtained when the geophones were buried at a depth of 10 m (on the left) and 50 m (on the right).

When we compared the CMP gather obtained from geophones buried at 10 m and 50 m depth, we observed that the ghosting from 50 m geophone depth is more pronounced compared to that obtained from the 10 m depth geophone (figure 10c). To investigate the nature of ghosting, we examined the frequency-dependent signal strength for the two different geophone depths. Figure 11 shows their amplitude spectra. We observed that the effect of ghosting limited the low frequency energy of retrieved seismic data from 50 m geophones, which are usually useful for imaging when the high frequencies are limited (Figure 11). To address the ghost problem observed from 50m geophones, we used the

combination of hydrophones and geophones. Since the dimension of the pressure and velocity recordings differs, we compensated for this differences by increasing their ratio to 1 (Appendix B). We then examined the frequency-dependent signal strength for the combination of the pressure and velocity recordings for buried geophones and the velocity recordings for the geophones at 10m depth. Figure 12 shows their amplitude spectra. We observed that the use of the combination of the hydrophone and geophone infills the loss of the low frequency energy observed in the retrieved seismic data from 50 m geophones (Figure 12). From these observations, we concluded that the frequency content of the deep "noise" sources in the field should be studied to dictate an optimal burial depth for geophones – a depth designed to minimize ghosting effects over that frequency band. However, the use of the combination of hydrophone and geophone would cancel the ghost effect observed for buried geophones. Nevertheless, to completely evaluate the effects of geophone depth, a viscoelastic modeling of a near surface that includes a weathered layer is necessary, as the benefit obtained by burying geophones beneath an attenuating zone may override any considerations of ghosting, and the ghosting path would experience that attenuation while the direct reflections would not

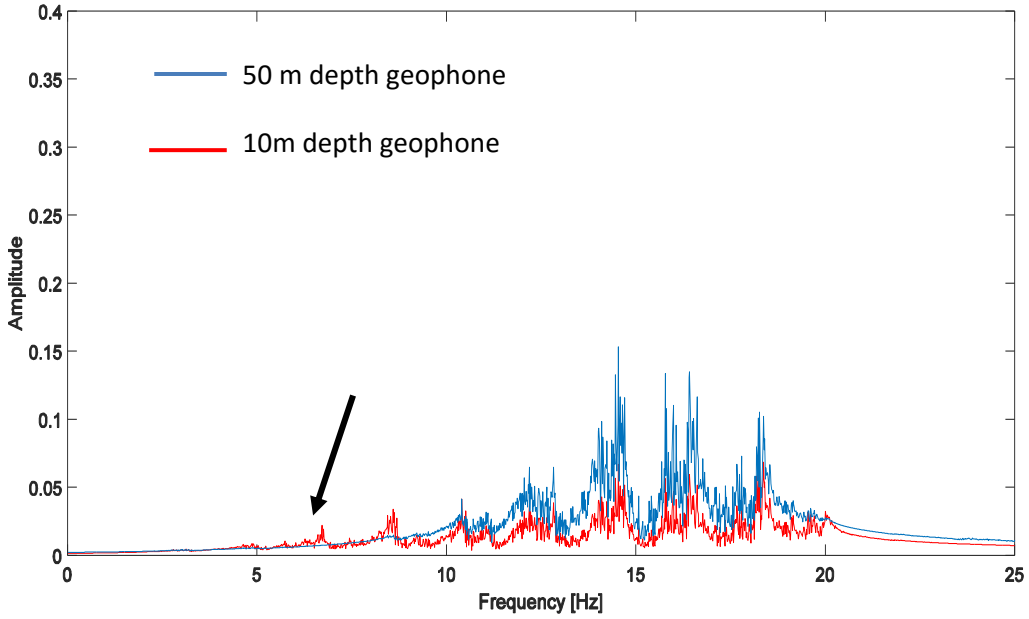

Figure 11: Amplitude spectra for seismograms from the different geophone burial depths, differentiated by color as indicated. The loss of low frequency energy of retrieved seismic data from 50 m geophones is indicated by the arrow.

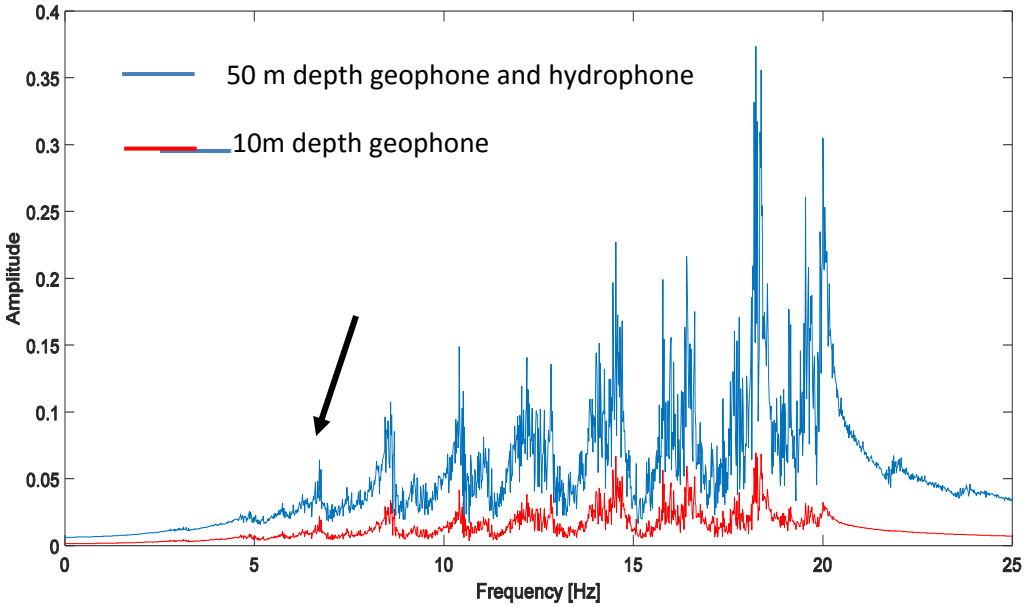

Figure 12: Amplitude spectra for seismograms from the different geophone burial depths, differentiated by color as indicated. The loss of low frequency energy of retrieved seismic data from 50 m geophones in figure 11 is regained from the use of the combination of hydrophone and geophone as indicated by the arrow here.

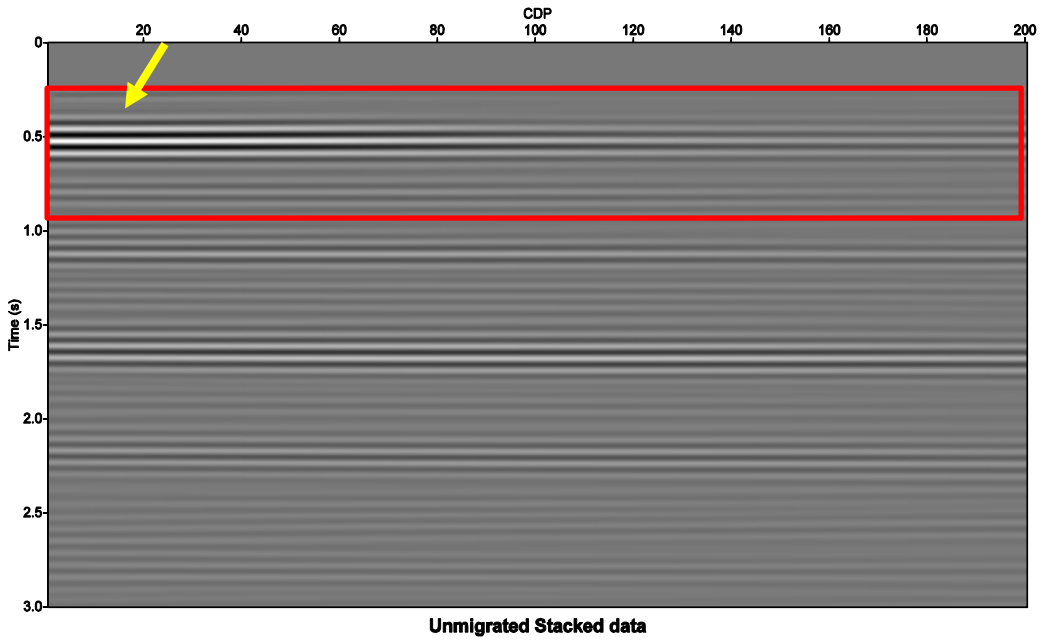

Figure 13: Unmigrated Stacked Section for geophone burial at 50m depth. Reflections at 0.5s arrival show poor temporal resolution due to ghost reflections limiting the low frequency energy. Compare with Figure 7, for 10m depth geophones.

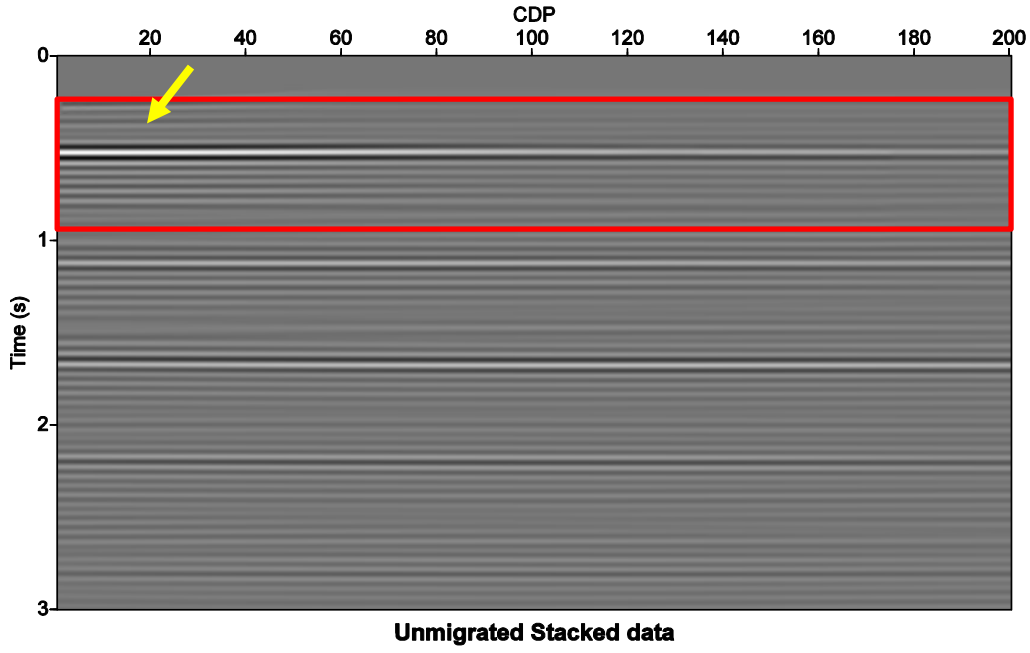

Figure 14: Unmigrated Stacked Section for geophone and hydrophone burial at 50m depth. Reflections at 0.5s arrival show high temporal resolution. Compare with Figure 13, for 50m depth geophones.

5.3. Influence of Shallow Noise Sources Generated at Shallow Depth on the Retrieved Reflection Data from Subsurface Sources

In this section, we study how shallow noise sources, intended to resemble coherent noise, affect retrieved reflections from deep sources. The sources generated in figure 2 are referred to as deep noise sources that might actually have tele-seismic origins or arise from local fluid injection at depth. The recovered reflections from these sources are the desired responses that we seek to observe. However, shallow noise sources generated at the shallow depth are commonly coherent across a geophone spread and arise from cultural (such as human motion, traffic, and industrial vibrations) or natural (such as wind and waves) sources, which commonly appear as high-frequency coherent ambient noise. To simulate this, we used shallow noise sources in the FD modeling, this time with a maximum frequency of 30Hz. The noise sources were randomly distributed between 100 m and 200 m depth, within the area covered by the geophone spread. Figure 15 shows the model that we used for the shallow noise sources.

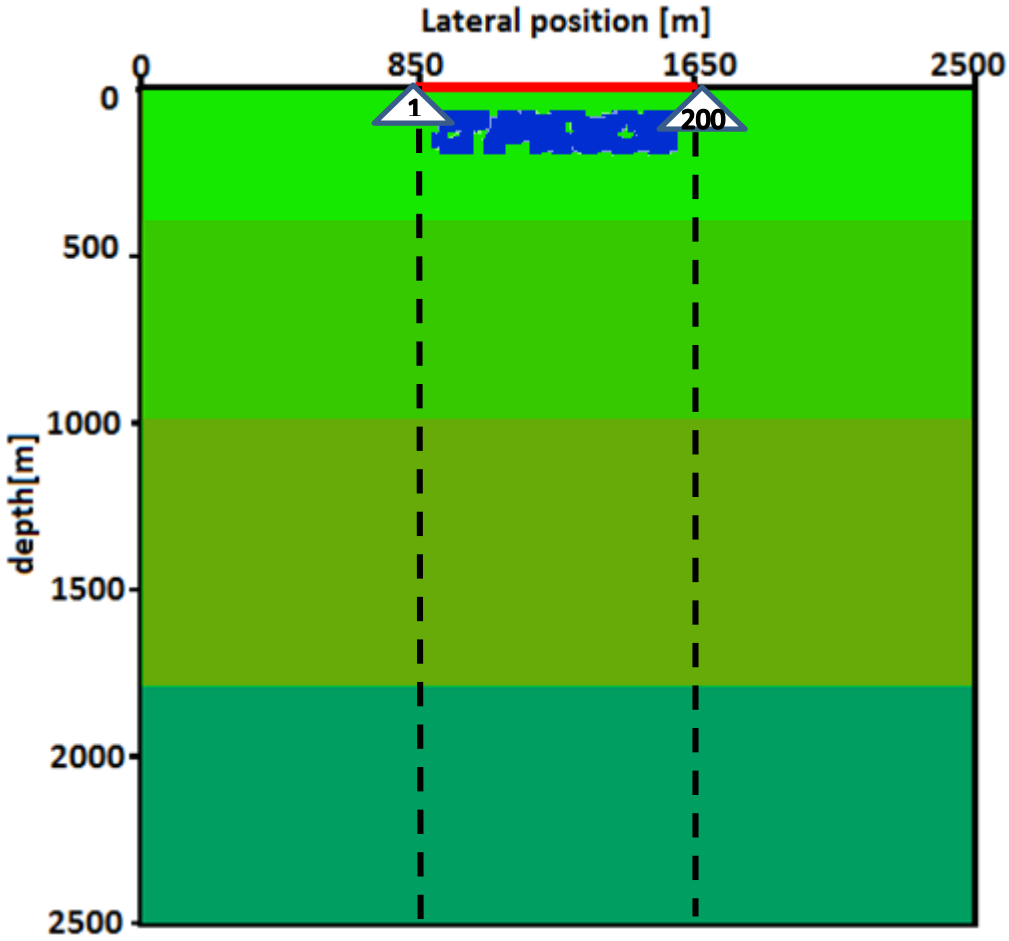

Figure 15: An acoustic model of the random source position at a shallow depth between 100m and 200m. The rest of the model is the same as in Figure 2, with geophones buried at 10m depth.

Following the same correlation process, as used for the deeper events to obtain common virtual-shot gathers, we summed (stacked) these with the common virtual-shot gathers obtained earlier from the deep noise sources. Figure 16 shows one common virtual-shot gather for the shallow noise sources, the deep noise sources, and after summation.

a)

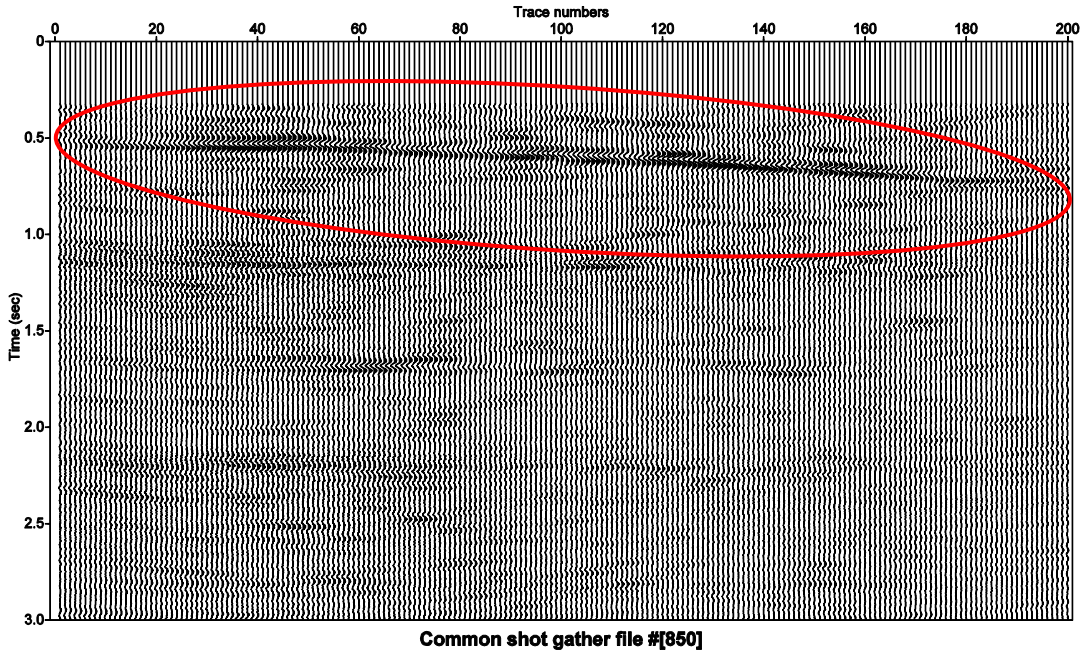
Trace numbers
0
20
40
60
80
100
120
140
160
180
200
Time (sec)
0
0.5
1.0
1.5
2.0
2.5
3.0
Common shot gather file #[850]

b)

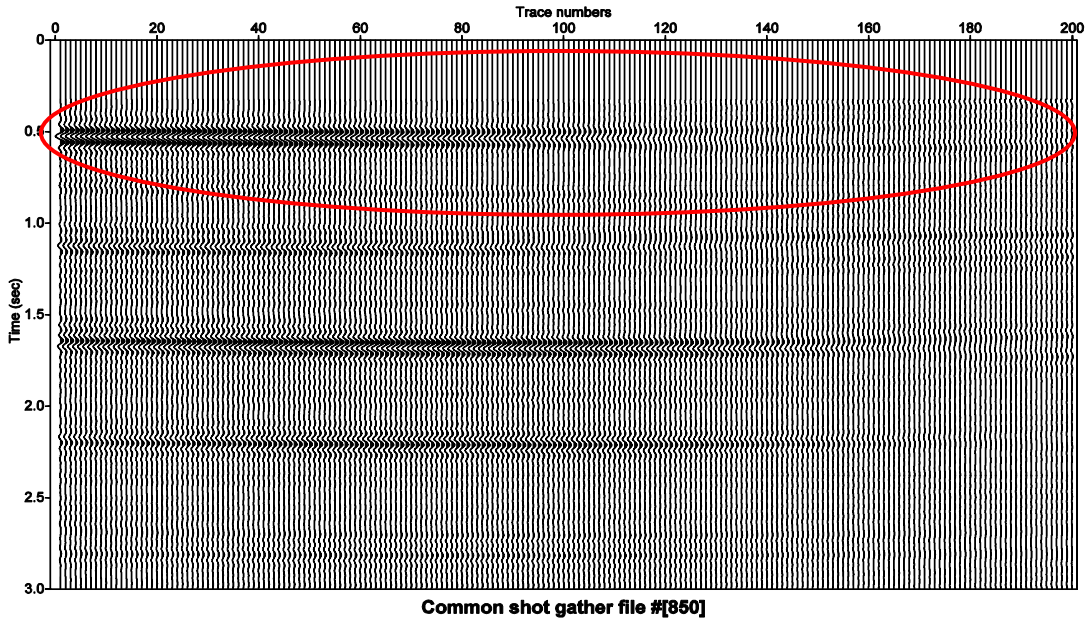
Trace numbers
0
20
40
60
80
100
120
140
160
180
200
Time (sec)
0
0.5
1.0
1.5
2.0
2.5
3.0
Common shot gather file #[850]

c)

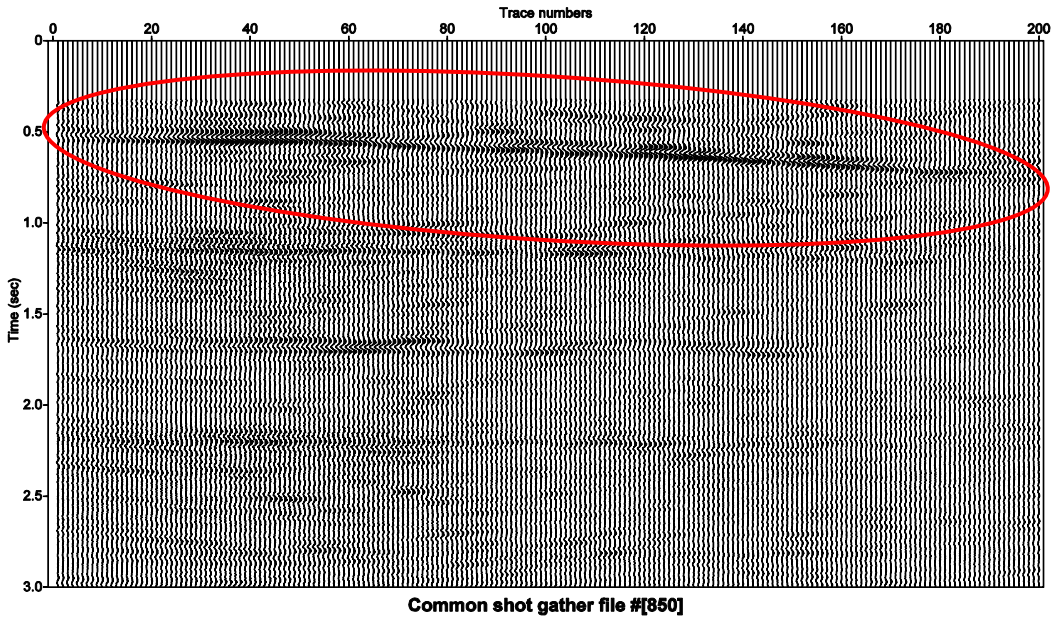

Figure 16: Comparison of the common virtual-shot gather at 850 m obtained for a) shallow noise sources b) deep noise sources c) summation of both shallow and deep noise sources. The red oval is used to emphasize the stronger moveout of the first interface as imaged by the shallow sources than by the deeper sources, and the large effect that shallow source gather has on the summed gather.

Comparing results shown in figure 16, we observed that figure 16c agrees with the horizontal media shown in figure 2. This observation also suggests that the strong reflections from the shallow noise sources (shown in figure16) dominate the summed common virtual-shot gathers. The summed common virtual-shot gathers retrieved were then sorted into CMP gathers and stacked after velocity analysis and NMO correction (Appendix C). Table 3 summarizes the stacking velocities, the predicted RMS velocity, and the model interval velocities.

Table 3: Comparison of the stacking velocity and the predicted RMS velocity for the summed shallow and deep noise sources.

Thickness of layer (m)	Depth to top of layer (m)	Time within the layer (s)	Interval Velocity (m/s)	Density (kg/m^3)	Stacking velocity at the base reflector (m/s)	Computed RMS velocity at the base reflector (m/s)
400	0	0.53	1500	1000	1494	1500.0
600	400	0.60	2000	1400	1583	1782.3
800	1000	0.55	2900	1500	2905	2211.3
700	1800	0.36	3900	1800	3929	2588.9

Figure 17 and 18 shows the CMP gather at number 1050 and the stacked section after velocity analysis.

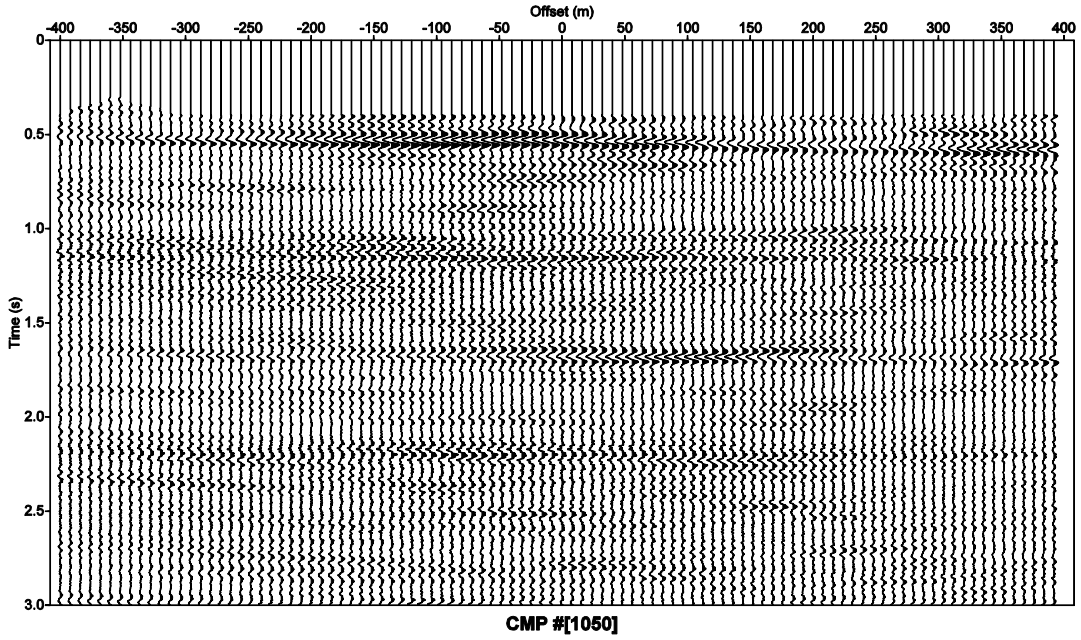

Figure 17: Common midpoint gather with time-dependent gain applied.

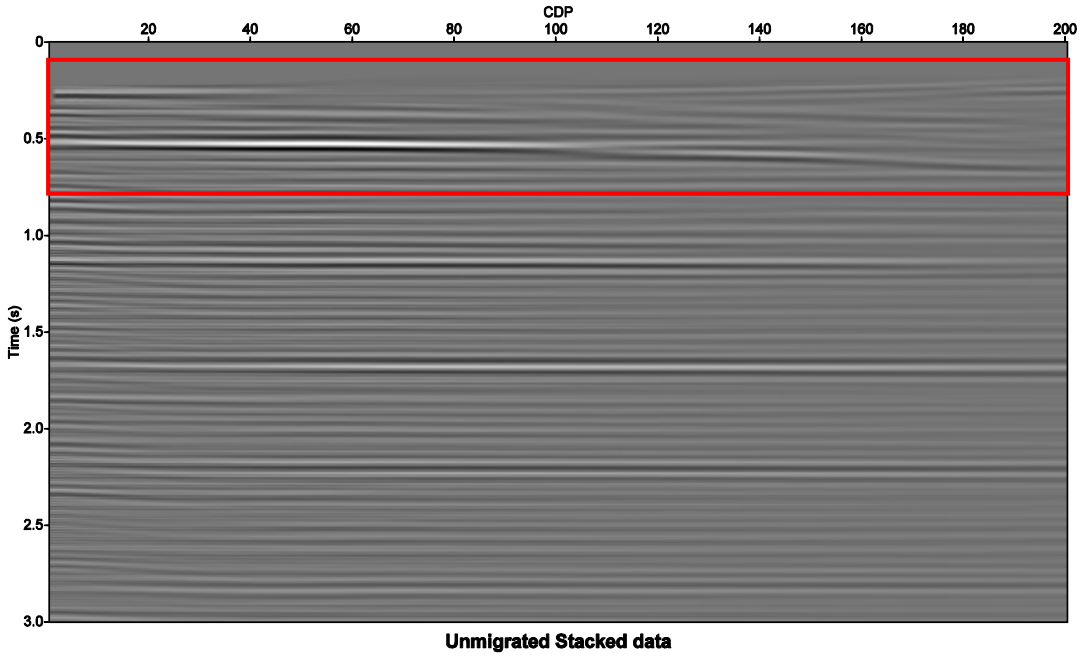

Figure 18: Unmigrated stacked section after velocity analysis and a time-dependent gain was applied. The reflection arrivals in the red box show distorted reflections compare to the deeper reflections below 1s.

5.3.1. Signal to Noise Ratio

The shallow noise sources, due to their proximity to the geophones, resulted in seismograms with very large amplitudes compared to those from the deep sources. Considering the distortion of the shallow reflection arrivals at 0.5s (figure 18), we examined the "signal-to-noise ratio" of the seismograms obtained after summing the deep and the shallow reflections. We assumed that the signals from shallow noise sources comprised the "noise" seismograms. We estimated the "signal-to-noise ratio" by first calculating the standard deviation of a given trace in the "noise" (shallow source) seismograms and the "signal" (deep source) seismograms (Appendix D). In this analysis, 20 traces were selected. For these traces, an average of the "signal-to-noise ratio" values

was found to be 0.084. To obtain "signal-to-noise ratio" values of 1 and 4, we increased the amplitude of the "signal" (deep source) seismograms by factors of 10.2 and 40.2. In the first case, the "signal-to-noise" ratio should be approximately unity, and in the second case, approximately 4:1. (In the original case, that ratio was 1:12; that is, the "noise" was 12 times the amplitude of the "signal.") The same procedure for estimating the "signal-to-noise ratio" was repeated for the resulting gathers, obtaining values of 0.86 and 3.4 respectively, close enough to our intended values to proceed. Figure 19 shows the comparison of the reflections arrivals obtained for these cases.

a)

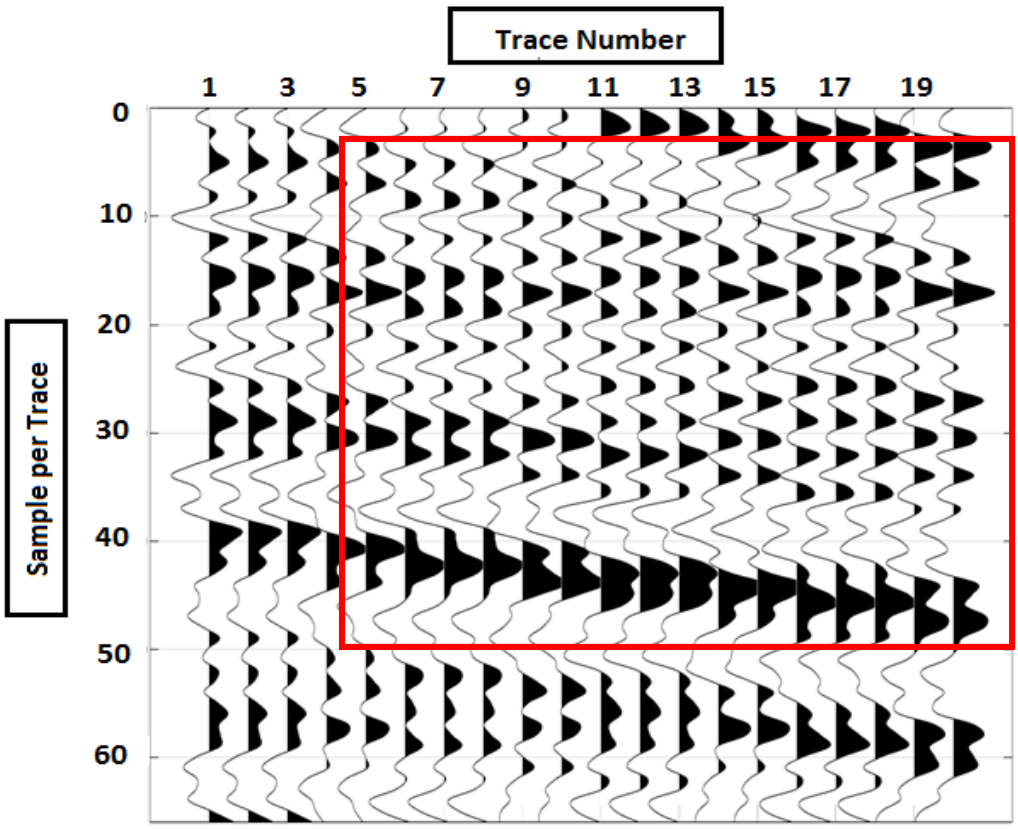
Trace Number
1
3
5
7
9
11
13
15
17
19
Sample per Trace
0
10
20
30
40
50
60

b)

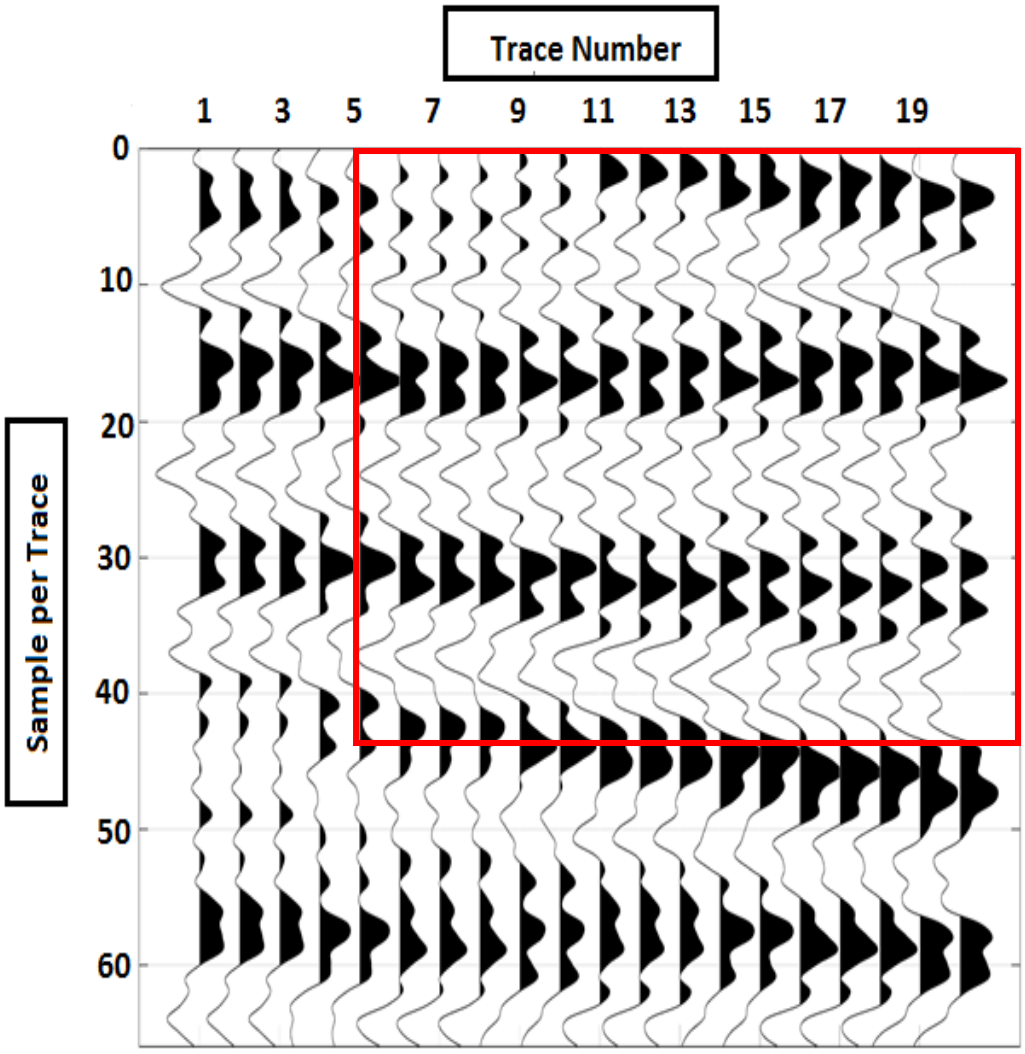
Trace Number
1
3
5
7
9
11
13
15
17
19
Sample per Trace
0
10
20
30
40
50
60

c)

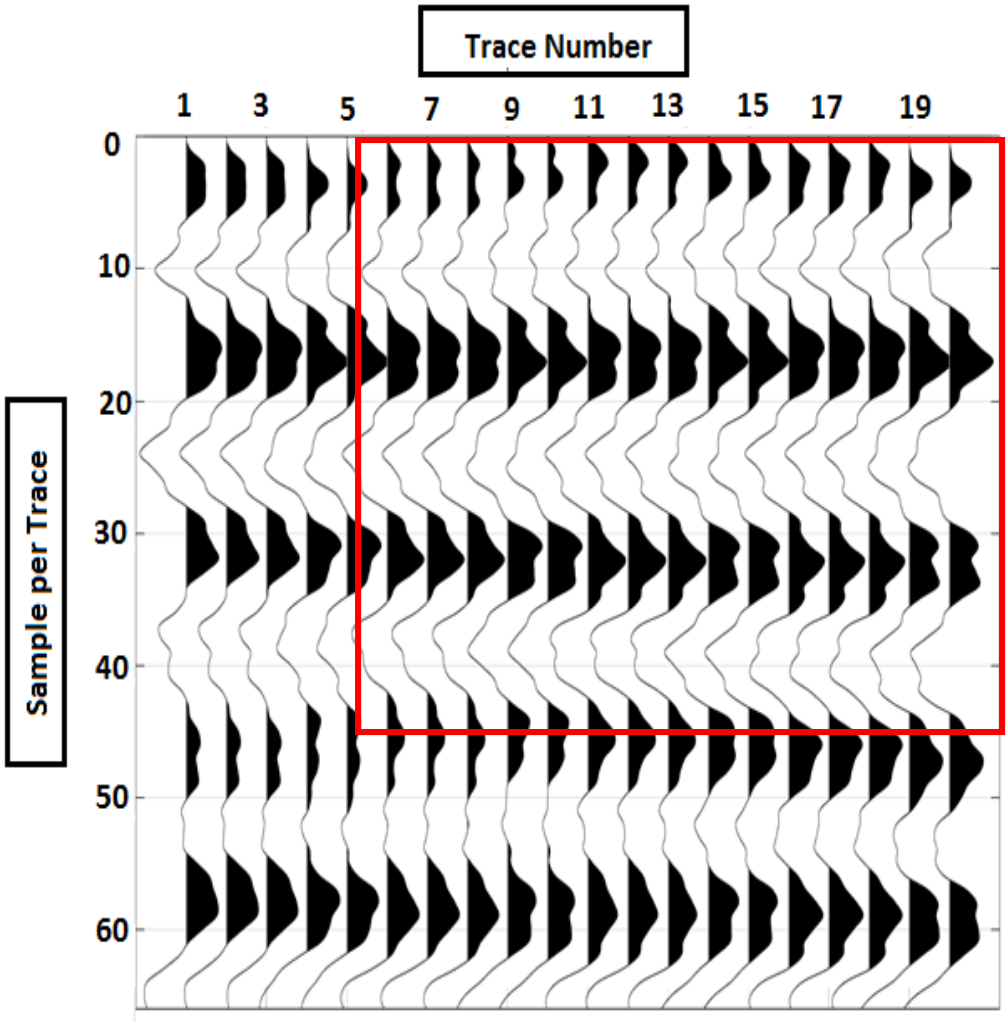

Figure 19: Comparison of retrieved common shot gather at 850 m with different "signal to noise" ratio of a) 0.085, b) 0.86, and c) 3.4. These results display 20 traces of 200 traces with 65 samples per trace for the signal to noise ratio. As is particularly evident for the trace segments in the red box, the quality of the retrieved reflections improves as the "signal to noise" ratio increases.

By comparing the gathers in Figure 19, we note that our retrieved reflections improve as the "signal to noise" ratio increases. Based on this observation, we used the highest "signal-

to-noise" gathers for the rest of the process. Figure 20 shows the CMP gather and the stacked section obtained after velocity analysis, NMO correction, and stacking.

a)

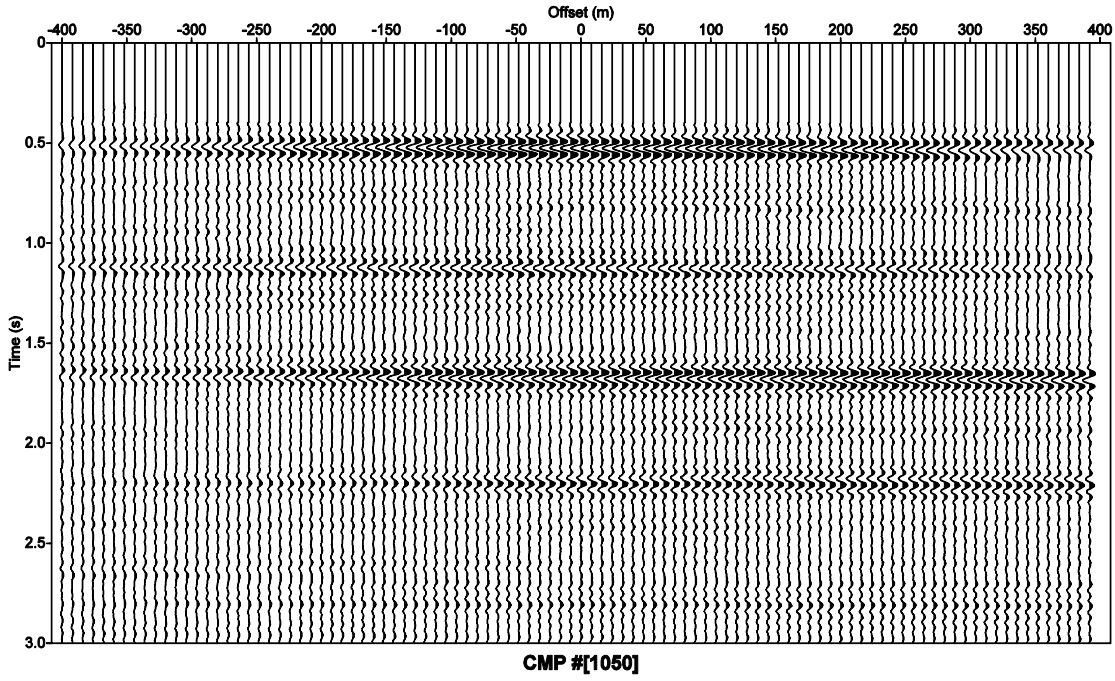

b)

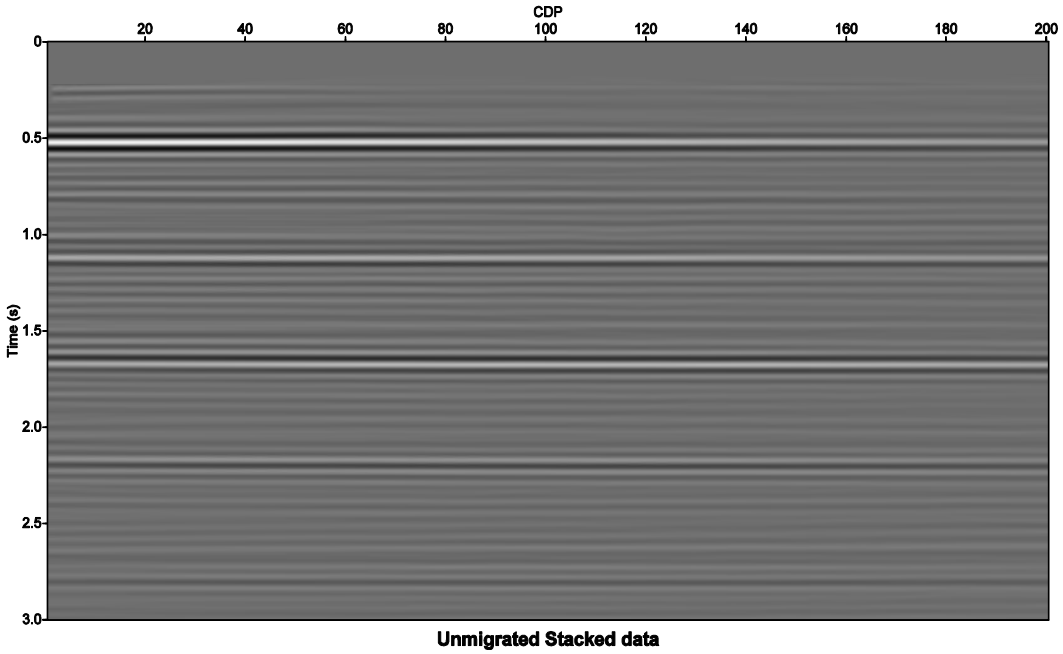

Figure 20: a) CMP gather when the "signal to noise" ratio was increased to 3.4. b) Unmigrated stacked section after velocity analysis, NMO correction, and stacking.

The seismic image obtained when "signal-to-noise" was 0.085 (Figure 19) and when increased to 3.4 (Figure 20) demonstrate that strong coherent signals from shallow noise sources have the potential to interfere destructively with our desired responses.

6. Conclusions

Passive measurements are considered cost efficient compared to active measurements in large part because passive measurements require no active source. To reconstruct reflection responses from transmission responses obtained from subsurface sources, the principle of seismic interferometry is applied and tested through numeric modeling. The retrieved responses (for reflections) are usually weak and poorly distinguished from other events. We studied various factors such as geophone interval, geophone depth, and effects of shallow noise sources and their influence on the quality of the retrieved reflections. We observed that geophone intervals had a negligible influence on the quality of the retrieved reflections, perhaps because the geologic structure is very simple. Studying the effects of geophone depth on the quality of the retrieved reflections, we observed the effects of ghost reflections after the first arrival. In this case, a shallower depth might provide us with a better result than a buried geophone, but the combination of geophone and hydrophone cancels the ghost effect observed when a buried geophone is used. In any case, a buried geophone under an attenuating weather layer is likely to improve the image both through avoiding the lossy path, but also through decreasing the amplitude of any ghosting signal. Finally, studying the effects of shallow noise sources on reflection responses obtained from deep sources, we observed that the strong events from those shallow noises can have a destructive effect on our desired reflections. Overall, our results emphasize the importance of data conditioning and processing techniques such as deconvolution and f-k filtering. Although these methods are beyond of study scope they are likely to improve the image for seismic interferometry, just as they do for active source imaging.

7. References

Arts, R, O Eiken, A Chadwick, P Zweigel, L Van der Meer, and B Zinszner. 2004. "Monitoring of CO 2 injected at Sleipner using time-lapse seismic data." *Energy* 29 (9):1383-1392.

Boullenger, B., A. Verdel, B. Paap, J. Thorbecke, and D. Draganov. 2015. "Studying CO2 storage with ambient-noise seismic interferometry: A combined numerical feasibility study and field-data example for Ketzin, Germany." *Geophysics* 80 (1):Q1-Q13. doi: 10.1190/Geo2014-0181.1.

Buchholtz, H. 1972. "A note on signal distortion due to dynamic (NMO) corrections." *Geophysical Prospecting* 20 (2):395-402.

Claerbout, Jon F. 1968. "Synthesis of a Layered Medium from Its Acoustic Transmission Response." *Geophysics* 33 (2):264-269. doi: 10.1190/1.1439927.

Harris, Jerry M., Richard C. Nolen-Hoeksema, Robert T. Langan, Mark Van Schaack, Spyros K. Lazaratos, and III James W. Rector. 1995. "High-resolution crosswell imaging of a west Texas carbonate reservoir: Part 1—Project summary and interpretation." *GEOPHYSICS* 60 (3):667-681. doi: doi:10.1190/1.1443806.

IEA. 2015. World Energy Outlook Special Report 2015: Energy and Climate Change. Paris, France: OECD/IEA.

Ivandic, Monika, Christopher Juhlin, Stefan Lueth, Peter Bergmann, and Artem Kashubin. 2013. "Geophysical monitoring of CO2 at the Ketzin storage site-the results of the second 3D repeat seismic survey." 75th EAGE Conference & Exhibition incorporating SPE EUROPEC 2013.

Lackner, Klaus S. 2003. "A guide to CO(2) sequestration." *Science* 300 (5626):1677-8.

Sherlock, Don, Aoife Toomey, Mike Hoversten, Erika Gasperikova, and Kevin Dodds. 2006. "Gravity monitoring of CO2 storage in a depleted gas field: A sensitivity study." *Exploration Geophysics* 37 (1):37-43. doi: doi:10.1071/EG06037.

Thompson, A Richard, James M Moran, and George W Swenson Jr. 2008. *Interferometry and synthesis in radio astronomy*: John Wiley & Sons.

Thorbecke, Jan W., and Deyan Draganov. 2011. "Finite-difference modeling experiments for seismic interferometry." *Geophysics* 76 (6):H1-H18. doi: doi:10.1190/geo2010-0039.1.

Wapenaar, K., and J. Fokkema. 2006. "Green's function representations for seismic interferometry." *Geophysics* 71 (4):Si33-Si46. doi: 10.1190/1.2213955.

Wapenaar, Kees, Deyan Draganov, Roel Snieder, Xander Campman, and Arie Verdel. 2010. "Tutorial on seismic interferometry: Part 1 — Basic principles and applications." *Geophysics* 75 (5):75A195-75A209. doi: doi:10.1190/1.3457445.

8. Appendices

Appendix A

a)

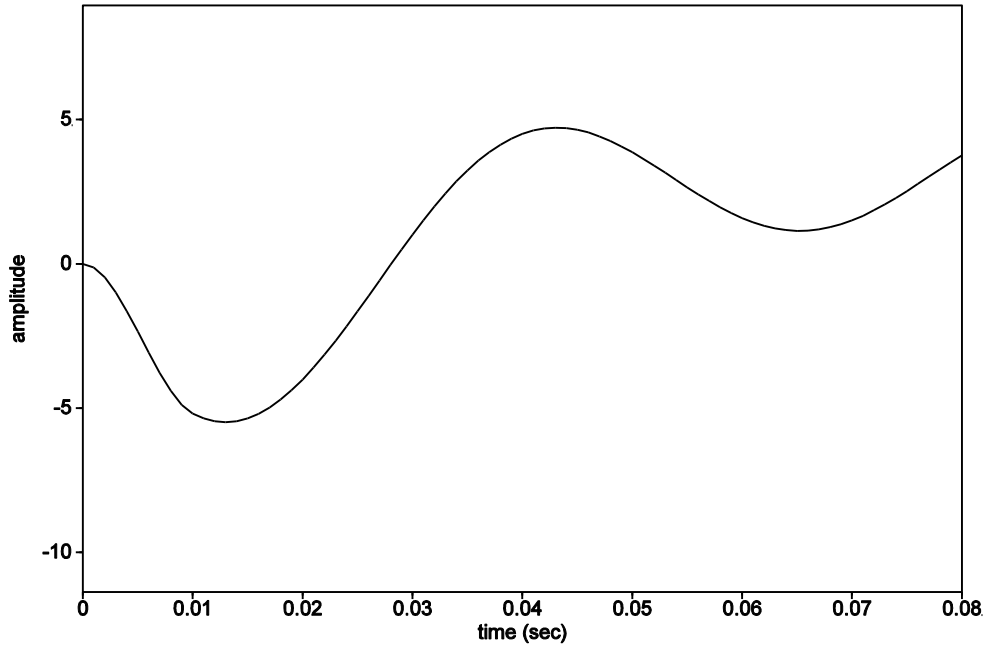

b)

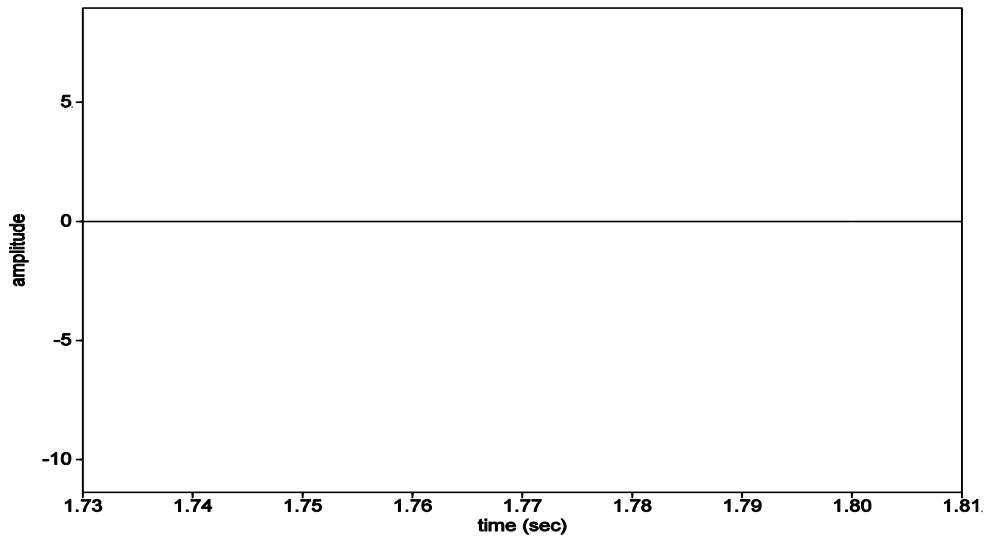

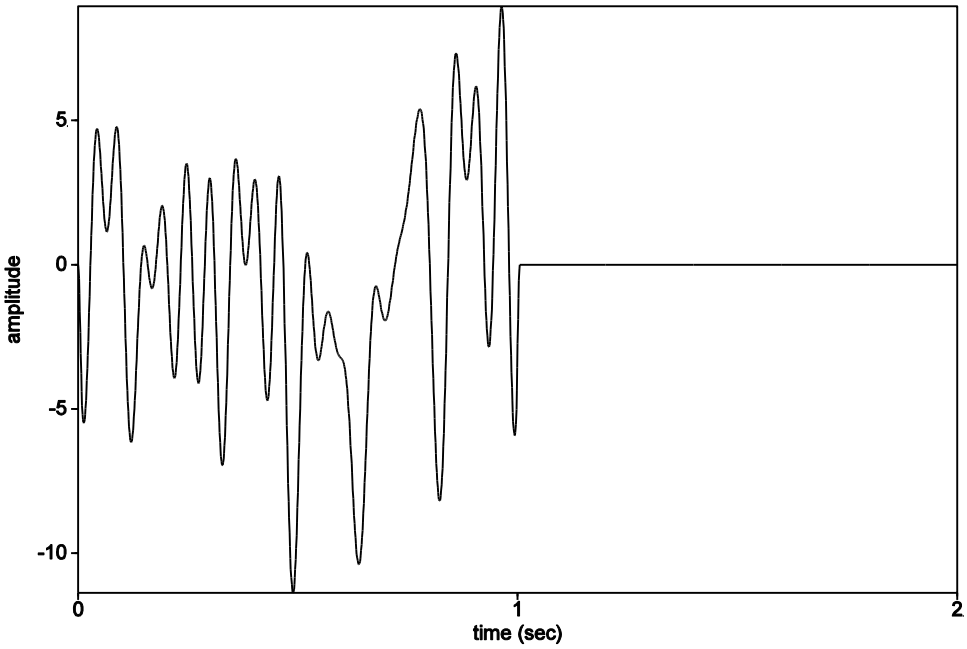

c)

Figure 21: The results in a) shows the beginning and b) shows the end of the signal amplitude presented in c.

Appendix B: Hydrophone and Geophone recordings at 50 m depth

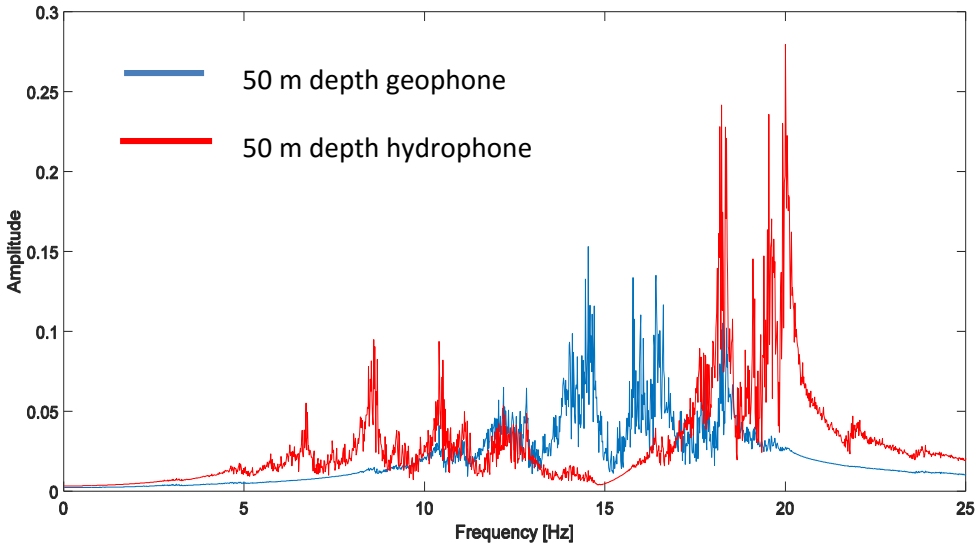

Figure 22: Amplitude spectra for seismograms from the hydrophone and geophone recordings, differentiated by color as indicated.

Appendix C: NMO correction

In the case of horizontal layers with constant velocity, Dix (1955) gave a two-way hyperbola time equation by

$$t^2(x) = t_o^2 + \frac{X^2}{V^2} \qquad Appendix\ C.1$$

where V is the velocity of the layer, t_o is the two-way travel time at zero-offset, and X is the offset.

In horizontal layering, the RMS velocity is defined as:

$$V_{RMS} = \sqrt{\frac{\sum_{i=1}^{N} \Delta t_i V_i^2}{\sum_{i=1}^{N} \Delta t_i}} \qquad Appendix\ C.2$$

V_i is the interval velocity of the ith layer, Δt_i is the vertical two-way travel time to the ith layer and N is the number of layers.

Note that this approximation is for small offset.

A hyperbolic equation can describe the normal moveout. Therefore, for NMO correction is:

$$\Delta t_{nmo}^2 = t^2(x) - t_o^2 \qquad Appendix\ C.3$$

Such an equation is fit to the moveout in gathers, to be used as the "stacking" velocity.

In an ideal case, the NMO velocity is identical to the RMS velocity, but in reality, it rarely is.

In the case of highly dipping beds, we correct for the effects of dip on the velocity before NMO correction; this is not needed for our model data in this study.

C3: Velocity analysis Results

a)

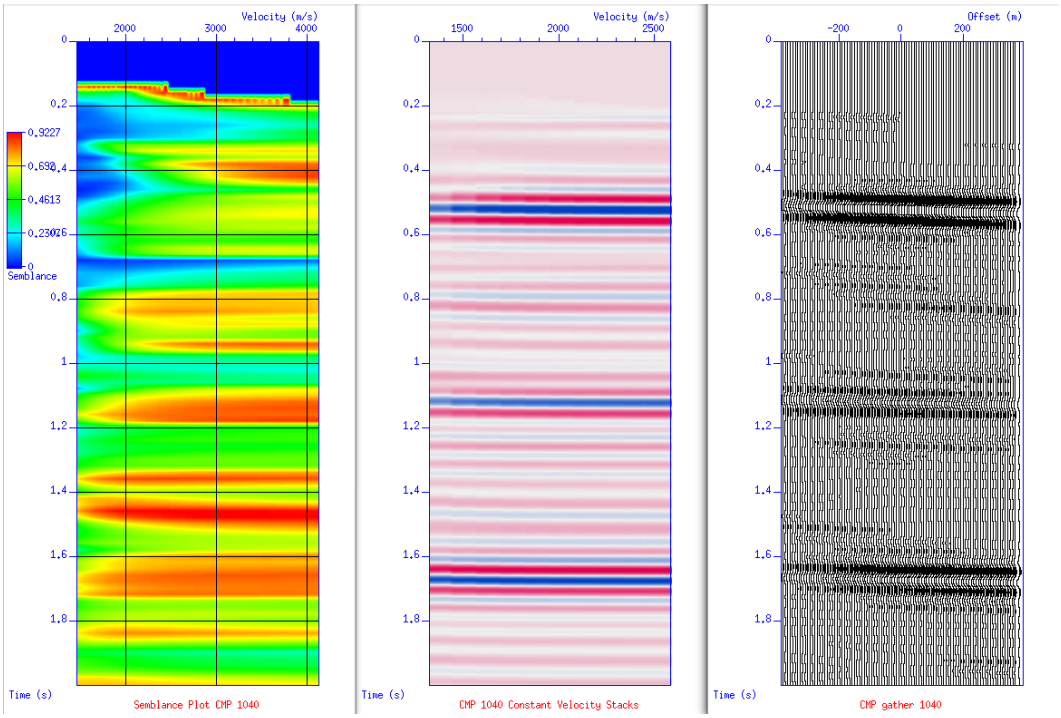
Velocity (m/s)
2000
3000
4000
0.9227
0.6920
0.4613
0.2307
0
Semblance
Time (s)
Semblance Plot CMP 1040
Velocity (m/s)
1500
2000
2500
Time (s)
CMP 1040 Constant Velocity Stacks
Offset (m)
-200
0
200
Time (s)
CMP gather 1040

b)

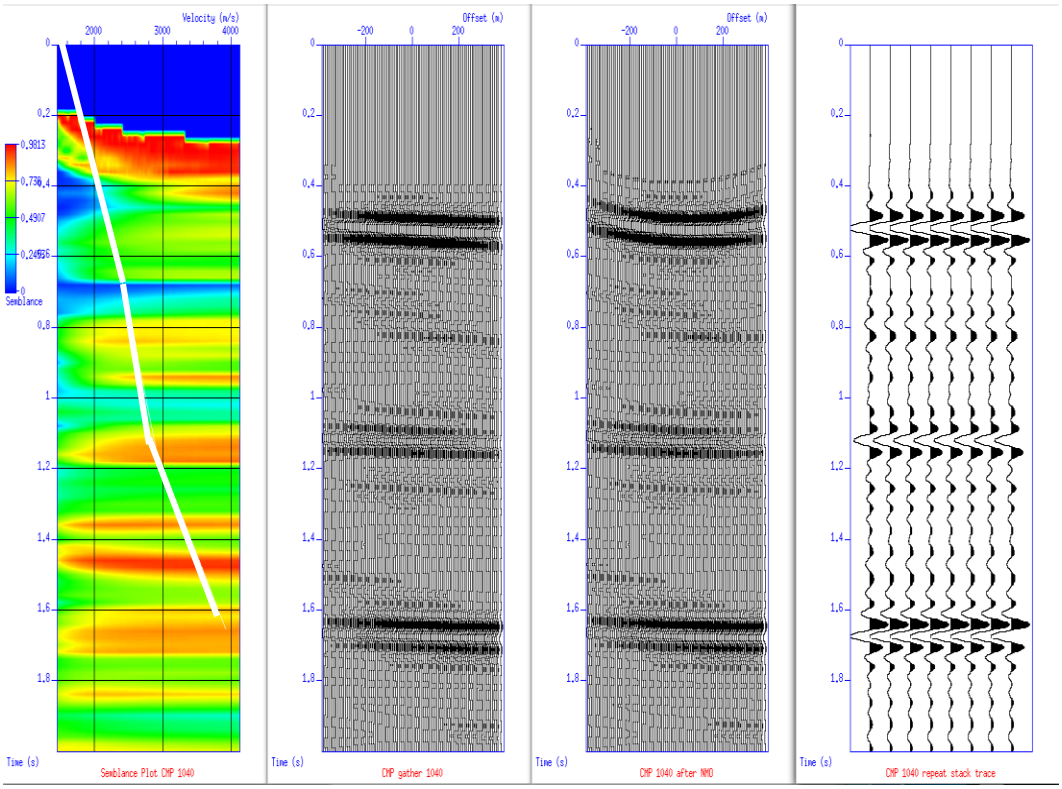

Figure 23: Example of Velocity Analysis for CMP gather 1040, for the original case of 10m depth and 4m interval, with deep sources. The result in a) shows the velocity spectrum contour plot, the semblance plot, and a CMP gather before velocity picking. The result in b) shows the velocity spectrum with the white line indicating the curve for NMO velocity, CMP gather before NMO correction, after NMO correction and a stacked gather for location 1040. The stacking velocities are 2251 m/s for the shallowest event and 2905 m/s and 3915 m/s for the deepest events.

Our gather in figure 1a is so flat due to the limited aperture used during modeling. This use of short aperture affected our velocity analysis in such a way that we had no constraint on the stacking velocities used in correcting the NMO thereby forcing us to pick velocities that are far from optimal for the shallowest event. However, this effect is not evident in the deeper events because their move-outs are so low that almost any velocities would flatten the events. Figure 3 shows an illustration of this effect.

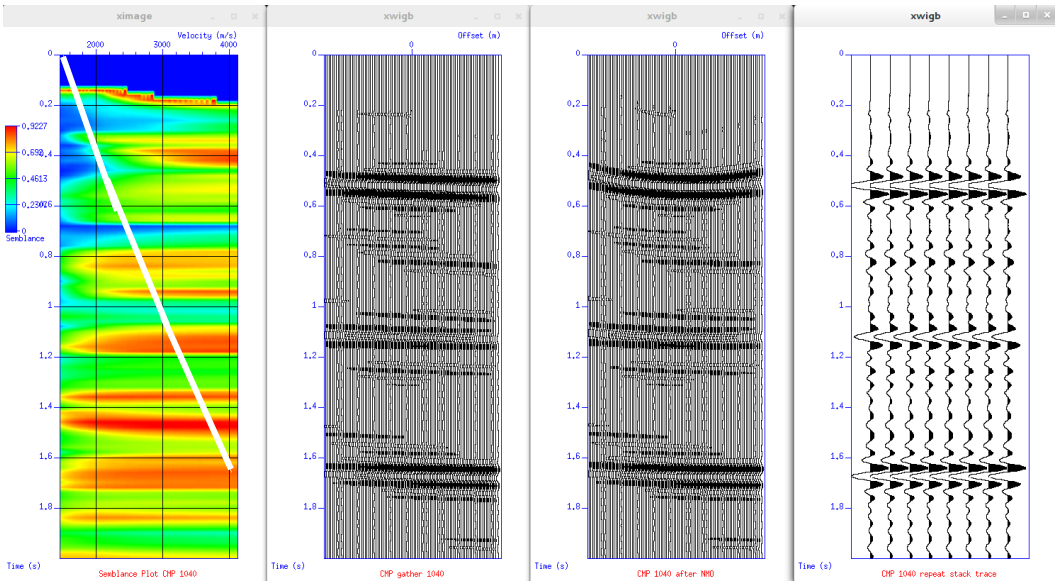

Figure 24: Example of Velocity Analysis for CMP gather 1040, for the original case of 10m depth and 4m interval, with deep sources. The result shows the velocity spectrum with the white line indicating the curve for NMO velocity, CMP gather before NMO correction, after NMO correction and a stacked gather for location 1040. The stacking velocities are 2251 m/s for the shallowest event and 3110 m/s and 4083 m/s for the deepest events.

Appendix D: Signal to Noise Ratio and Standard Deviation

D.1. Standard Deviation

For a vector A made up of N number of observations, the standard deviation is defined as

$$STD = \sqrt{\frac{1}{N-1}\sum_{i=1}^{N}|A_i - \mu|^2} \qquad Appendix\ D.1$$

where μ is the mean of A

$$\mu = \frac{1}{N}\sum_{i=1}^{N} A_i \qquad Appendix\ D.2$$

C.2.Signal to Noise Ratio

Signal to noise ratio for n number of columns in the vector A

$$SNR_i = \frac{STD_{signal}}{STD_{signal}} \qquad Appendix\ D.2.1$$

$$\overline{SNR} = \frac{\sum_{i=1}^{i=n} SNR_i}{n} \qquad Appendix\ D.2.2$$

where $\overline{SNR}$ is mean of SNR over n number of columns in the vector A